

## A. SPECIFIC AIMS

The overall goal of this project is to develop new pulse sequences and methods of structural and perfusion MRI to support the research projects and clinical applications of the Resource Center. For conventional MRI methods, the detection of neurodegenerative diseases (ND) remains a challenge. Limited signal and contrast to noise ratios are major obstacles to measure subtle brain abnormalities with high precision. In addition, the complexity of ND, including structural, functional, and metabolic abnormalities requires a multivariate imaging approach. Over the past decade, the investigators of this project have developed a suite of new MRI acquisition and RF pulse methods resulting in higher efficiency, sensitivity, and precision. The current application is an extension of these previous efforts and represents the combined efforts of these investigators to develop improved acquisition techniques focused on the detection of neurodegenerative diseases. The specific aims are:

**Aim 1: Development of Multi-acquisition Variable T1-weighted Imaging (VTI) for Resolving Voxel Compartmentation and Enhancing Resolution:** Resolution limits of MRI and the corresponding partial volume problem constrain precise measurements of structural alterations. Utilizing the different T1 values of brain tissue, we aim to overcome partial volume effects in structural MRI by developing multi-acquisition variable T1-weighted imaging (VTI), an approach that provides T1 profiles, i.e. multiple T1 rates of image voxels from which voxel compartmentation can be predicted. VTI is made possible by accelerated parallel imaging, allowing rapid acquisitions of MPRAGE data with variable inversion periods or FLASH data with variable flip angle sets within clinically acceptable scan times (<30 min). We aim to optimize precision without sacrificing acquisition speed by considering flip angle variations, transmit field imperfections, and noise bias. Furthermore, we will develop physical and statistical models to accurately estimate the T1 profiles, yielding voxel compartmentation as well as T1 maps of the brain with diminished partial volume confounds and ultimately enhanced resolution. Our efforts for VTI will specifically be tailored towards precise measurements of cortical thinning and gray matter loss to enhance sensitivity for detection of diseases. **Specifically, we propose the development of:**

1. **T1 estimations by least-squares (LS) fits with spatial priors to stabilize the estimations through regional support. We expect that LS fits with spatial priors for jointly estimating the maps will substantially improve the precision of subvoxel classification compared to the traditional approach in doing the fits independently for each voxel.**
2. **A new multi-acquisition method for subvoxel T1 measurements by varying BOTH the flip angle  $\alpha$  as well as the RF pulse spacing  $\tau$ , in order to achieve a better signal diversity which will allow us to optimally estimate  $T_1$ .**
3. **A new deblurring method for MPRAGE, allowing greater flexibility for acquiring the transient magnetization on its way to steady state in order to achieve higher image contrast and SNR. Since the blurring depends to a large extent on T1, we propose to take advantage of the abundant T1 information of T1-weighted data for the search of the optimal deblurring value. We achieve convergence in solving the deblurring problem by jointly minimizing the total variation in T1 and intensity maps upon cycling iteratively through image reconstruction, deconvolution, and T1 estimations and then re-estimating the deblurring value using the new T1 estimations.**

**Aim 2: Development of Quantitative Evaluations of Cerebral Blood flow and Water Uptake into the Brain:** While arterial spin labeling (ASL) in combination with volumetric (3D) gradient-and-spin-echo (GRASE) acquisitions have improved sensitivity to measure cerebral blood flow (CBF), quantification of CBF remains a challenge. Furthermore, local susceptibility effects resulting in geometrical and signal distortions at high magnetic fields can compromise measurement precision.

1. **Improved Modeling of ASL Signal Dynamics:** We aim to quantify cerebral blood flow and water uptake into the brain from multiframe 3D ASL GRASE with dual and multiple-echo acquisitions - as developed in project 2 of this Acquisition Core. This will be accomplished by incorporating into a distributed compartment model of brain perfusion the temporal evolution of both T1 and T2 relaxation of the ASL signal.

2. **Correction of ASL Signal Distortions:** To further improve precision of CBF measurements using 3D-ASL-GRASE, we will design paired 3D GRASE acquisitions with forward/reversed-gradients to remove geometrical and intensity distortions due to local background gradients. To remove the distortions, we will develop a procedure based on dynamic time warping to accurately resolve dissimilarities between image pairs of forward/reversed-gradient GRASE acquisitions.
3. **Easy-to-Use Software for ASL Image Processing:** We will develop an easy-to-use ASL-software package for processing of 3D ASL-GRASE and computation of parametric 3D maps of blood flow and water uptake into the brain.

Achievement of the aims of these projects will establish a set of protocols that can be used to develop imaging markers of neurodegeneration for the purpose of early diagnosis and monitoring progression of these diseases. These projects will also benefit a large number of funded ongoing collaborative and clinical research studies.

## B. BACKGROUND AND SIGNIFICANCE

**B.1. The Need for Improved Structural MRI:** Neurodegenerative diseases (ND) are generally associated with brain tissue loss, especially of gray matter in the cortex<sup>(1)</sup>. The ability to detect abnormalities of gray matter is therefore of great clinical importance. However, to image gray matter is problematic. First, the cortex, where most gray matter is contained, is a very thin sheet, typically 2-4mm. Moreover, the cortex itself is heterogeneous and consists of 5 to 6 sublayers, which may selectively be affected by various ND<sup>(2)</sup>. Second, the cortex is also a highly convoluted structure that folds back on itself in an unpredictable manner. Therefore, to precisely delineate the cortex one must obtain images with high-spatial resolution in all directions. Despite substantial progress, resolution limits of conventional MRI remain a major obstacle to accurately delineate the cortex, not to mention resolving the cortical sublayers.

Over the years, the development of specialized pulse sequences<sup>(3,4)</sup>, fast gradient switching coils, and navigator pulses<sup>(5)</sup> has greatly improved MRI quality. In addition, short repetition time gradient spoiled MRI sequences were developed that provide fast acquisitions in three dimensions (3D), such as fast low flip angle FLASH<sup>(6)</sup>, magnetization prepared rapid gradient echo (MPRAGE)<sup>(7)</sup>, and modified driven equilibrium Fourier transform (MDEFT)<sup>(8)</sup>. Moreover, 3D acquisitions are more efficient in terms of signal-to-noise ratio (SNR) per time than slice selective 2D scans, because data acquired at every image formation step (phase-encodings) contribute to the signal. Perhaps most importantly, the magnetic field strength of MRI systems has dramatically increased over the years and sensitivity improved. The benefit of higher magnetic fields for image resolution is now well established for 3T and 4T systems<sup>(9-11)</sup>. Since T1 relaxation times of gray and white matter diverge with increasing magnetic field<sup>(12)</sup>, while T2 times slightly converge<sup>(13)</sup>, T1-weighted sequences, like FLASH, MPRAGE, and MDEFT, have become the choice of volumetric brain imaging at high magnetic fields. As a result, whole brain imaging with 1 mm<sup>3</sup> or slightly better resolution is now fairly common practice. Despite this progress, limited MRI resolution remains a major obstacle to detecting neurodegenerative abnormalities in the cortex and cortical sublayers. A further complication for resolution is the partial volume effect (PVE), whereby a single voxel can contain variable amounts of gray matter, white matter, and cerebrospinal fluid (CSF). Although volumetric errors from PVE may globally average to zero, locally the errors can be substantial and distort measurements of brain structures<sup>(14)</sup>. A higher resolution would reduce – though not necessarily eliminate – the PVE and possibly improve sensitivity to detect gray matter loss. However, increasing MRI resolution comes at a heavy cost of rapidly declining SNR. The loss of SNR with higher resolution can in principle be recovered by prolonging the acquisition time  $t$ . The relationship between  $t$  and resolution  $\Delta x$  is well understood. Without reference to specific imaging techniques, Mansfield and Morris<sup>(15)</sup> have shown that  $t$  must increase with the 6<sup>th</sup> power of  $\Delta x$  to maintain SNR, or more formally

$$t \propto SNR^2 (T_1/T_2) f^{-7/2} (\Delta x)^{-6} . \quad (1.1)$$

Here,  $T_1/T_2$  is the ratio of longitudinal to transverse relaxation times, which generally increases with field strength and  $f$  is the MRI resonance frequency, which is directly proportionate to field strength. The steep rise in acquisition time to offset the loss of SNR from higher resolution is a major barrier for clinical studies to practically increase MRI resolution beyond a certain point. For example, to double image resolution in all

directions from say  $1.0 \times 1.0 \times 1.0 \text{ mm}^3$  - which requires about 8 minutes using MPRAGE - to  $0.5 \times 0.5 \times 0.5 \text{ mm}^3$  without sacrificing SNR would require an 8 ½ hr acquisition, clearly an impractical approach. A more efficient solution to increase MRI resolution and overcome PVE is highly desirable.

Given the practical limits for higher MRI resolution, many new pulse sequence developments have focused on enhancing image contrast rather than increasing resolution to better delineate certain brain structures, especially the cortex<sup>(16,17)</sup>. However, a higher image contrast may not reduce PVE nor does it enhance resolution. On the contrary, contrast enhancement is often accomplished by re-arranging the k-space trajectory relative to the inversion-recovery period of the signal, potentially introducing deleterious effects on the MRI point spread function that can diminish resolution if left uncompensated<sup>(18,19)</sup>. On the other hand, PVE reductions can be accomplished with single and dual inversion recovery sequences by carefully tuning the inversion periods to selectively suppress for instance white matter and CSF while maintaining the gray matter signal or vice versa, i.e., to suppress gray matter and CSF while maintaining the white matter signal<sup>(20)</sup>. Although single and dual inversions have led to some interesting clinical applications, notably for Parkinson's disease<sup>(21)</sup>, the effectiveness for eliminating PVE is limited to brain regions with uniform T1 relaxation. In cases of non-uniform T1 values, signal suppression is either compromised or experiments have to be repeated with different single/dual-inversion values, a great inefficiency since no SNR is gained with this approach despite repeated acquisitions.

In this proposal, we aim to determine PVE rather than to suppress it with the goal of measuring subvoxel compartmentation. The information may ultimately be helpful to enhance resolution. The goal is accomplished by developing rapid multi-acquisition variable T1-weighting imaging (VTI) to capture the T1 profiles, i.e. multiple T1 decays in an image voxel. Since gray matter, white matter, and CSF are characterized by different T1 values and water exchange between the tissues is negligible on the time scale of MRI, multiple T1 relaxations hold information about voxel compartmentation. Physical or statistical models of VTI modulations can be used to extract this information. VTI may be obtained in a number of ways, including variable flip angle FLASH or MPRAGE with variable inversion times. Rapid FLASH and MPRAGE acquisitions will be made possible by new parallel imaging methods with high acceleration factors, developed in the Reconstruction Core, while new algorithms for subvoxel segmentation will be developed in the Processing Core. While the principles of VTI are not new and variable flip angles FLASH has been used before to obtain T1 maps of the brain<sup>(22-25)</sup>, the previous applications were not aimed at resolving PVE or subvoxel compartmentation.

The ultimate goal of VTI, though not a specific aim of this proposal, is to eventually enhance MRI resolution. An enhancement is in principle possible, because information about voxel composition together with prior knowledge of the smoothness of the brain can be exploited in a Bayesian approach to compensate for insufficient imaging data. Although enhanced image resolution has been an active area of research over the past two decades, mainly motivated by new video technologies<sup>(26,27)</sup>, its application to MRI has stirred some controversy<sup>(28-32)</sup>. Earlier attempts to enhance MRI resolution focused on subvoxel shifting, but the possible enhancement was equivalent to zero-padding. It was suspected that the narrow band-limit of voxel shifting with conventional MRI, i.e. 100-200Hz per pixel, prevented an effective gain in resolution<sup>(32)</sup>, especially in presence of fast  $R2^*$  rates of signal decay, causing blurring. It should be noted that the idea to enhance resolution promoted here is completely different. First, the information extracted from VTI is not subject to band limits and thus less sensitive to  $R2^*$  blurring and second, brain smoothness has been shown to constitute a realistic prior for a Bayesian formulation of the image reconstruction problem<sup>(33)</sup>. These efforts for VTI will specifically be tailored towards precise measurements of cortical thinning and gray matter loss that are expected to enhance sensitivity for detection of diseases.

**B.2. The Need for Improved Measurements of Cerebral Blood Flow:** The assessment of brain function via cerebral blood flow (CBF) is considered to be extremely useful for early detection and diagnosis of ND. Furthermore, the relationship between functional and structural alterations in the brain, whether concurrent or dissociated, may provide additional valuable information for ND staging<sup>(34)</sup>. Project 2 of the Acquisition Core will develop improved methods for efficient 3D mapping of CBF via arterial spin labeling (ASL) under the direction of Dr. Feinberg. Recently, 3D imaging of the ASL signal has become possible, providing higher SNR efficiency than conventional 2D techniques, because data acquired at every step for image formation contributes to the ASL signal<sup>(35-37)</sup>. Furthermore, 3D ASL imaging facilitates measuring the time course of the ASL signal simultaneous throughout the brain, in contrast to sequential measurements with 2D techniques. The development of 3D ALS techniques has been complicated by the demand for fast single-shot acquisitions

while avoiding geometrical distortions and signal loss but Feinberg et al. <sup>(35)</sup> developed a fast 3D mapping technique, based on GRASE <sup>(4)</sup> to tackle both problems. The gain in sampling efficiency of 3D ASL-GRASE can be used in several ways, including higher spatial or temporal resolution. Furthermore, the combined acquisition of gradient and spin-echo acquisitions in 3D GRASE allows in principle a fast mapping of the T2 evolution of the ASL signal. This could be especially attractive for studies of water uptake into the brain.

**B.2.a. Unique Possibility to Study Water Uptake into the Brain and Blood Brain Barrier:** The possibility to use ASL-MRI for studies of the uptake of water into the brain and thus permeability of the blood-brain barrier (BBB) could have great value for assessing ND. Dysfunction in the BBB underlies a number of widely spread diseases, such as AD <sup>(38-40)</sup>, PD <sup>(41)</sup>, and multiple sclerosis <sup>(42)</sup>. Currently, BBB disruption is measured with MRI by bolus injection of a contrast enhancing agent, such as gadolinium. However, gadolinium and similar contrast agents have substantial molecular weights and large hydrated radii that usually prohibit diffusion through the barrier. Thus, contrast MRI is mainly an indicator for massive damage of the BBB but not particularly sensitive to subtle alterations to diffusion of small molecules, such as water. There is no current MRI method to quantify the barrier to diffusion of small molecules. 3D ASL-GRASE has ideal pre-requisites to measure the kinetics of water uptake into the brain. First, sampling efficiency of 3D ASL-GRASE is much higher than with 2D techniques and therefore, measurements of perfusion kinetics can be performed with high temporal and spatial resolution. Second, the transverse magnetization of the ALS-signal in 3D ASL-GRASE is predominantly governed by T<sub>2</sub> relaxation, thus providing better spatial localization for the perfusion signal than EPI-bases sequences that are depend on T2\*. Moreover, the possibility using multiple-echo 3D ASL-GRASE to capture the temporal variation of T2-relaxation of the ASL signal while perfusing into the brain could be a breakthrough in capturing the dynamics of water uptake and BBB. Previous MRI studies of BBB permeability relied solely on T1-relaxation <sup>(43-45)</sup> or were confounded by T2\* relaxation <sup>(46)</sup>. Estimating water uptake from the dynamics of T1-relaxation is complicated since the entire signal evolution under T1-relaxation before the uptake has to be taken into account. Similarly, estimating water uptake from T2\* is complicated, because field distortions due to macroscopic background gradients and vascular effects, such as BOLD, can obscure modulations of T2\*. In contrast, T2 does not dependent on the history of the signal and furthermore, is to a large extend insensitive to background gradients and BOLD. Dual echo 3D ASL-GRASE raises therefore the possibility that changes in the BBB can be detected in diseases, even though no gross disruption of the barrier may be measurable with gadolinium MRI.

BBB permeability can be extracted from modeling the time course of the ASL. Models have been based on pharmacokinetic information, such as exchange of blood water between capillaries and brain tissue and the Bloch-Terry equations, which describe spin magnetization in the presence of relaxation and flow <sup>(44,45,47-54)</sup>. However, early models in ASL-MRI <sup>(47-49)</sup> were based on single-compartment kinetics for water, despite H<sub>2</sub><sup>15</sup>O PET studies demonstrating a finite rate of water diffusivity across the BBB <sup>(55-58)</sup>. Moreover, an instantaneous equilibrium between blood and brain water was assumed, which is also a gross simplification <sup>(59)</sup>. More recently, two conceptually different models have been proposed for water diffusion through the BBB, assuming a restricted exchange between intra- and extra-capillary compartments: One model assumes well-mixed water concentrations in each of the two compartments <sup>(44,54)</sup>. The other model, also known as a distributed model, accounts for a concentration gradient of ASL water along the capillary path (or along both intra- and extra-capillary spaces) <sup>(45,53)</sup>. While the first model is limited to uniformly distributed labels, the latter model may not be applicable in practice, since parameters, such as capillary length, etc. are not accurately known <sup>(45)</sup>. Furthermore, both models, while focusing on the effect of restricted water exchange, did not systematically include additional effects, such as dispersion of ASL bolus duration. Although the general model for ASL proposed by Buxton et al <sup>(51)</sup> considered dispersed bolus durations the assumption was made that water is freely diffusible <sup>(60)</sup>. Recently, we proposed a comprehensive model for ASL, which takes into account variable transit times, bolus durations, distributed concentrations of capillary water and restricted BBB permeability <sup>(61)</sup>. However, our previous analysis was limited by 2D ASL acquisitions which could not facilitate simultaneous measurements of the time course of the ASL signal from all regions in the brain. In addition, multiple-echo acquisition to assess T2 relaxation of the ASL was not available with 2D acquisitions and also would have been less efficient than in 3D. In this proposal, we plan to refine our four phase model for acquisitions using 3D ASL-GRASE and furthermore will incorporate the temporal T2 evolution into the model to improve the estimation of water uptake into the brain. We expect that the additional information from 3D and multi-echo acquisitions will greatly improve quantification of perfusion measurements.

**B.2.b. The Need for Accurate Corrections of Geometry and Intensity Distortions:** While the increased sensitivity provided by 3D ASL-GRASE should greatly improve quantification of CBF and water uptake into the brain, geometrical and intensity distortions in the image induced by background gradients can substantially compromise precision, especially when 3D ASL-GRASE is performed at high spatial resolution. As the linear correspondence between spatial location and MR resonance frequency is lost, straightforward Fourier transform of the data obtained through such incorrect mapping results in images with distortions in geometry and intensity (arising from voxel shift and signal loss, respectively). Since susceptibility scales linearly with the magnetic field, distortions become a more prominent problem at higher magnetic fields. EPI is particularly vulnerable to field imperfections, because the bandwidth for phase encoding is relatively narrow and accumulative phase-errors can quickly dominate the evolution of the EPI signal. In contrast, 3D GRASE is less vulnerable to distortions, since the EPI trains within GRASE are shortened and cumulative phase errors are self-regulated by spin-echo refocusing pulses<sup>(4)</sup>. Parallel imaging provides an additional benefit, since fewer phase-encoding steps are required and thus less phase errors accumulate<sup>(62)</sup>. Nonetheless, the distortions cannot be eliminated even when 3D GRASE and parallel imaging are combined. Additional corrections are required to estimate how an image may look undistorted. Numerous attempts have been made to remove distortions by image-based post processing, including free form deformations using cubic B splines<sup>(63,64)</sup> and affine transformation<sup>(65)</sup>, or histogram matching<sup>(66)</sup> to a baseline image. However, post-processing methods are approximations, which may not capture the full extent of distortions. In addition, post-processing provides only a relative correction, since a baseline image can also be distorted. Another approach, though not mutually exclusive to post-processing, is the measurement of the displacement field, which causes the distortions and then use of this information to reconstruct images without these distortions. This is also known as the inverse problem approach to correct for image distortions<sup>(67)</sup>. The two most prominent concepts in this field are the field mapping and the reversed-gradients methods.

**B.2.b.i. Field Mapping Methods:** Field-mapping methods rely on measurements of field non-uniformity and then translate field distortion into voxel shifts that compensate the distortions<sup>(68)</sup>. A major shortfall of this approach is apparently that field maps can also be distorted and therefore only relative distortions can be corrected, similar to post-processing techniques. Though conjugate phase methods in conjunction with field maps<sup>(69)</sup> have been widely used for distortion corrections, they rely on the assumption that the displacement field is spatially smooth. It is, however, clear that this assumption is often invalid at tissue boundaries, where sharp transitions can occur. Moreover, the need to unwrap the phase makes the problem nonlinear, involving a binary decision for each voxel. Iterative conjugate gradient methods circumvent the assumption of smoothness<sup>(70)</sup>, but a straightforward implementation of the conjugate gradient algorithm suffers from inconveniently long processing times. Another field-mapping method called simulated phase evolution rewinding (SPHERE)<sup>(71)</sup> uses a distortion kernel to rewind the phase accumulated from field inhomogeneities. In this method, two EPI images are collected at different echo times from which the field map is derived. The calculated field map and an initial estimate of the image are used to calculate the distortion kernel. The whole process is the k-space equivalent of using the field map to reverse pixel shifts in the image space. However, the performance of SPHERE is dependent on the initial estimate of the image and it can fail for large field inhomogeneity. Another method that is more indirectly associated with field mapping is called point-spread function (PSF) mapping method<sup>(72)</sup>, which consists of acquisitions with additional phase encoding gradients applied in order to obtain PSF of each voxel. The distorted data is de-convolved with these PSFs to obtain undistorted images. The PSF approach is furthermore based on the assumption that the k-space sample locations are unaffected, which does not always hold because the k-space trajectory may be distorted by variations in the displacement field. In summary, while conjugate phase methods have widely been used for distortion correction, they rely on a number of assumptions that are often invalid in practice. Conjugate phase methods also do not correct for intensity variations. Finally, and perhaps most important, it has been shown that it is not possible to reconstruct the true image from a single EPI acquisition, even with perfect knowledge of the displacement field, because there is an irreversible undersampling of the signal from areas where the background gradient collaborates with the phase-encoding gradient of EPI<sup>(73)</sup>. Reversed gradient methods overcome this shortfall.

**B.2.b.ii. Reverse Gradient Methods:** In reversed-gradient methods, two EPI images are collected under equivalent imaging settings except that once traversing k-space bottom-up and once bottom-down, resulting in

two images with identical magnitude distortions in opposing directions<sup>(73,74)</sup>. These two images, together with a model for the image formation process allow estimating the underlying displacement field and undistorted images. The principle used for this calculation is that the images in the distorted and undistorted space are related through a transformation as long as the distortions do not exceed a certain threshold. Although sampling efficiency is cut in half with reverse gradient methods due to the acquisition of image pairs, this may not be a disadvantage when signal average is paramount. Although reverse-gradient methods have several advantages compared to field-mapping methods, including they do not rely on field-maps (which themselves are associated with distortions) and they generally outperform conjugate gradient methods even with a small number of iterations<sup>(67)</sup>, a major limitation of conjugate gradient method is a high computational demand. This can quickly grow astronomically as the dimensions of the kernel matrix for the conjugate gradient method grows with the square of the number of pixels, i.e., 128 x 128 images already require 4 Gb storage, approaching quickly the current storage limit of conventional computer systems. Therefore, alternative reconstruction methods with less computational demands are desirable. Dynamic Time Warping (DTW) is such a method.

**B.2.b.iii. Potential of Dynamic Time Warping (DTW):** DTW is an efficient matching procedure, initially used for speech recognition<sup>(75)</sup> that owes its power to quickly converge to the match by minimizing total error. The use of DTW as matching technique for MRI was initially proposed by Kannengiesser et al.<sup>(76)</sup>. So far, it has been used only for gradient-echo sequences, where the equality of integrals holds good for comparing the corresponding readout lines in two images. Care has to be taken while extending this method to EPI, because the complex phase evolution along with the unavoidable data truncation may violate the assumption of equality of integrals between reverse-gradient images. However, this is expected to be less of a problem for GRASE, because the sequence combines spin and gradient echoes to reduce geometrical distortions and signal loss. The method is also simpler than iterative conjugate phase and gradient method, because it only requires matching the sums of two images. Moreover, the computational dimensionality of DTW only increases proportionate to the image size, in contrast to a quadratic increase for conjugate gradient methods, an important consideration for the large data size of 3D ASL-GRASE. For all these reasons, we propose to develop DTW as the method of choice to correct for geometrical and intensity distortions, especially for volumetric ALS perfusion images at high resolution, i.e. a matrix size 128 x 128 x 32 or higher.

## C. PRELIMINARY RESULTS

**C.1. The Investigators of this Project:** Dr. Schuff worked on the development of 3T and 4.7T MR systems for Varian and Bruker before joining this group in 1993. After he joined this group, he developed single voxel, PRESS, and multislice spectroscopic imaging sequences that are widely used in this laboratory and by several other research sites throughout the world<sup>(77,78)</sup>. Dr. Schuff has also developed quantitative analyses of MRSI data, based on co-analysis with anatomical MRI data and linear regression statistics<sup>(78)</sup>. More recently Dr. Schuff in collaboration with Drs. Zhu and Jahng developed improved MRI perfusion methods using arterial spin labeling. ASL perfusion results on AD, other dementias, and mild cognitively impaired subjects have been published<sup>(79)</sup>. In addition, Drs. Schuff and Jahng developed new ASL perfusion techniques<sup>(80,81)</sup>, such as DIPLOMA (*d*ouble *i*nversions with *p*roximal *l*abeling of *b*oth tagging and control *i*mages)<sup>(82)</sup> and IDOL (*i*n-plane slice-selective *d*ouble inversion of *b*oth the control and the *l*abeling scans) that are aimed to reduce ASL imperfections. In addition, Drs. Schuff and Zhu developed an extended kinetic model for ASL to obtain quantitative measures of cerebral blood flow and water permeability of the blood brain barrier<sup>(43)</sup>. Since installation of a 4T system, Drs. Schuff and Stables optimized high-resolution structural MRI to study subfields of the hippocampus<sup>(83)</sup>, implemented pulsed and continuous ASL MRI (continuous ASL courtesy of Dr. Dedre, U Pennsylvania), and installed and improved <sup>1</sup>H EPSI<sup>(84)</sup> at 4T. In addition, pulsed ASL sequences based on 3D GRASE<sup>(35)</sup>, providing volumetric measurements of brain perfusion in 30 seconds were implemented in collaboration with Dr. David Feinberg (AMT). Other scientist of this project include:

- **Dr. Ashish Raj** has been working on MR reconstruction and segmentation problems for well over 5 years. He has become an expert in solving inverse problems and graph cuts algorithms. He is also the PI of the parallel imaging project in the Reconstruction Core.

- **Dr. Wang Zhan** recently joined the UCSF faculty. He has extensive experience in MRI pulse programming and developing analysis techniques. In addition, he has extensive experience in deconvolution from his passed work in EEG.
- **Dr. Xiaoping Zhu** is radiologist and MRI physicist. Dr. Zhu has been working extensively for the past 15 years in the field of contrast enhanced MRI, especially on cerebral blood flow modeling. Since joining this group in 2000, Dr. Zhu worked on the development of new pulse sequences for MR spectroscopy and perfusion, introduced deformation shape modeling to improve MR spectroscopy data processing and also developed new models for arterial spin labeling.

**C.2. Current MRI scan protocol used at 4T:** Currently, our 4T MRI protocol for patients and controls includes the sequences listed below. Since installation of the 4T system in January 2004, we have scanned more than 200 subjects and volunteers. The entire scan protocol lasts about 1hr and 10 min, including time for adjustments and shimming. It is tolerated by about 90% of the subjects: The protocol includes:

1. **T1-weighted 3D MPRAGE** for tissue segmentation (Scan Time= 5min 17s); Slices= 176; TR/TE= 2300/3.37ms; TI= 950ms; Voxel Size= 1.0x1.0x1.0mm; parallel imaging= GRAPPA with an acceleration factor of 2;
2. **T2-weighted Turbo Spin-Echo** for tissue segmentation and intracranial volume measurement (Scan Time= 3m 06s); Slices= 54; TR/TE= 8390/70ms; Voxel Size= 0.9x0.9x3.0mm; parallel imaging= GRAPPA with an acceleration factor of 2;
3. **Fluid Attenuated Inversion Recovery ( 3D FLAIR)** for identification of white matter lesions (Scan Time= 7min 37s); Slices= 120; TR/TE= 5000/355ms; TI= 1900ms; Voxel Size= 1.0x1.0x2.0mm
4. **Susceptibility-Weighted Imaging (3D SWI)** for measurements of brain iron and vessels (Scan Time= 6min 21s); Slices= 56; TR/TE= 25/32ms; Voxel Size= 0.6x0.5x1.2mm
5. **High-Resolution Turbo Spin-Echo** for measurements of hippocampal subfields (Scan Time= 6min 56s); Slices= 24 ;TR/TE= 3990/21ms; Voxel Size= 0.5x0.4x2.0mm.
6. **Diffusion tensor imaging (DTI)** using spin-echo echo-planar imaging (EPI) for mapping the diffusion signal in 2D (Scan Time= 1min 20s four times for averaging); Slices= 40; TR/TE= 6000/77ms; Voxel Size= 2.0x2.0x3.0mm; 6 direction for the diffusion sensitizing gradients; parallel imaging= GRAPPA with an acceleration factor of 2; **Recently, we added diffusion spectrum imaging (DSI) with 512 spherically arranged q-space samples within 15 min scan time. Dr. Wedeen's project in the Processing Core will develop methods to process and analyze DSI data.**
7. **Continuous arterial spin labeling (ASL-MRI)** for measurements of blood flow in 2D (Scan Time= 7min 06s); 1.0mm thick labeling band; postlabeling delay time= 1800ms; Slices= 16; TR/TE= 5200/9ms; Voxel Size= 5.0x3.8x5.0mm; **Recently, we added pulsed ASL 3D GRASE perfusion imaging with 12 different post-labeling delays for measurements of perfusion dynamics. Total scan time is 10 minutes.**

### **C.3. Variable T1-weighted Imaging (VTI)**

**C.3.a. Variable flip angle FLASH and variable inversion time MPRAGE imaging:** We have conducted initial experiments for VTI using FLASH with variable flip angles or MPRAGE with variable inversion-recovery times to test the dynamic range of T1 contrast changes and SNR. The currently implementation was performed with standard GRAPPA<sup>(85)</sup> parallel imaging with an acceleration factor of 2, yielding 3D FLASH images in about 2:50 minutes and 3D MPRAGE images in 5:17 minutes. Representative VTI images are shown in Figure 1. Several important observations can be made from these preliminary data: 1) This demonstrates that a consistent change in T1 contrast can be achieved at 4T with both FLASH and MPRAGE. Although the dynamic range of T1 contrast changes is larger for MPRAGE than for FLASH, FLASH may be more efficient in terms of the sampling rate of multiple image frames per unit time. 2) Effects from flip angle errors are visible in FLASH and also impact MPRAGE, emphasizing the importance of use of RF pulses with better immunity to B1-inhomogeneity and of accounting for flip angle errors. 3) SNR was sufficient even with acquisitions as short as 3 min and 5 min for FLASH and MPRAGE, respectively. This suggests that there is room for higher accelerations of at least another factor two, permitting acquisitions of 12 3D MPRAGE or 30 3D FLASH within

30 minutes and thus acquiring VTI data as proposed in this application. Figure 2 shows a parametric T1 map obtained from 9 FLASH frames with variable flip angle acquisitions, indicating our experience with T1 mapping.

### **C.3.b. T1 maps from multiple scans with variable flip angles (Schuff, Stables):**

This data was presented in the site visit. In a first attempt to jointly optimize VTI acquisition and T1 estimations, we performed FLASH experiments with a range of flip angle values. We particularly investigated the optimal trade off between SNR and large dispersion of flip angles for fitting T1. In Figure 2 are shown T1 maps derived from VTI acquisitions with (A) high SNR but a narrow range of flip angles ( $5^{\circ}, 10^{\circ}, 12^{\circ}$ ) versus (B) a lower SNR but a wide range of flip angle values ( $1^{\circ}, 10^{\circ}, 20^{\circ}$ ). In (C) are shown results using the full range of suitable flip angles ( $1^{\circ}-40^{\circ}$ ). A regular non-linear least squares (LS) algorithm was used to estimate T1, assuming homogeneous voxel compositions. As expected, widening the range of flip angle values stabilizes the fits better than high SNR. Over-determination of the fits, i.e. by collecting the full range of flip angles, reduces noise in the parameter estimations further. These results indicate the importance of jointly optimizing VTI acquisition and T1 estimations.

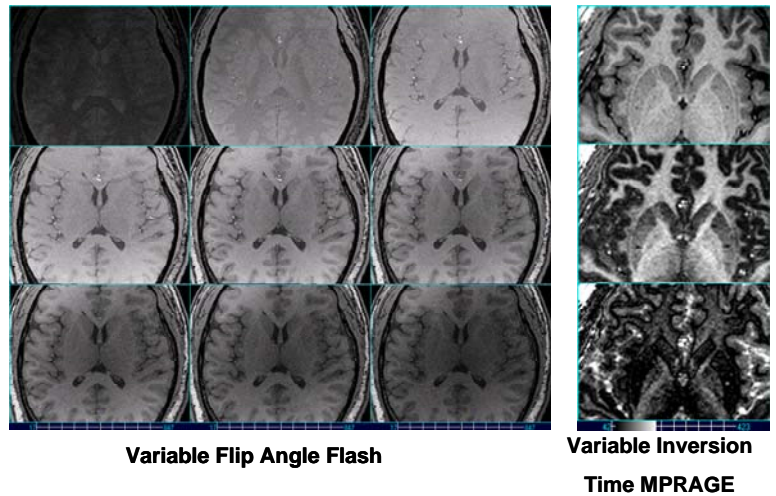


Figure 1: Variable T1-weighted Images

**C.3.c. Stabilization of T1 Estimations using spatial support (Dr. Raj):** Preliminary data on the earlier proposed estimation method (varying the flip angle only) are shown in Figure 3. The data demonstrates the effect of using spatial priors and jointly estimating the maps, compared to doing the LS fit independently for all voxels. The data shown was obtained from a simple quadratic smoothness prior (known as 1<sup>st</sup> order Tikhonov regularization). In these examples we used only 2D priors. Figure 3a shows fitting under no spatial prior and 3b under a quadratic spatial smoothness prior. The images are in pseudo-color, with the red channel denoting T1 values and the green channel denoting density values. Notice the improvement in SNR of (b) compared to (a). However, we wish to extend this to 3D in order to impose spatial priors in 3D and even more powerful spatial priors with edge-preserving properties of the form discussed in the Reconstruction Core project 3 (PI Raj).

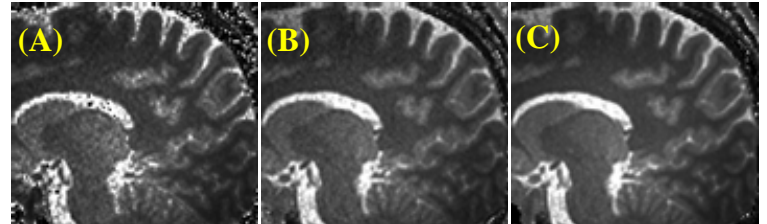


Figure 2: T1 estimations from variable flip angles

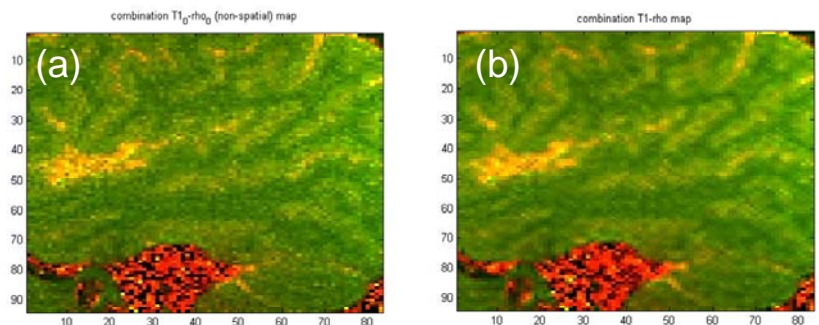


Figure 3: Effect of Using Spatial Priors for T1 Estimations

**C.3.d. MPRAGE Simulations (Drs. Matson, Zhan, Schuff):** We performed simulations of MPRAGE (MatMRI by Dr. Matson) to better understand the effects of acquisition parameters on SNR, contrast,

and image blurring. Figure 4 depicts evolutions of the longitudinal magnetization  $M_z$  toward steady state for the inner loop of MPRAGE, which consists of serial short  $\alpha$  pulses and phase-encoding along one direction in k-space. The vertical dashed lines in the figures indicate when the central part of k-space is encoded. Fig 4a depicts a typical MPRAGE setting at 4 Tesla in which sampling of the center part of k-space is delayed until all three tissue classes reach approximately steady state conditions (gray matter (red), white matter (green), and CSF (blue)). While blurring is largely avoided in this setting, SNR and contrast are sacrificed. There are several possibilities in MPRAGE to increase SNR and contrast, but most require relaxing the steady state condition for the signal, as shown in Figures 4b and 4c. However, a drifting signal leads inevitably to image blurring. Another approach is varying the flip angle  $\alpha$  during the RF pulse train, as shown in Fig. 4f to flatten the signal response, as shown in Figures 4d and 4e for  $M_z$  and  $M_{xy}$ , respectively. In

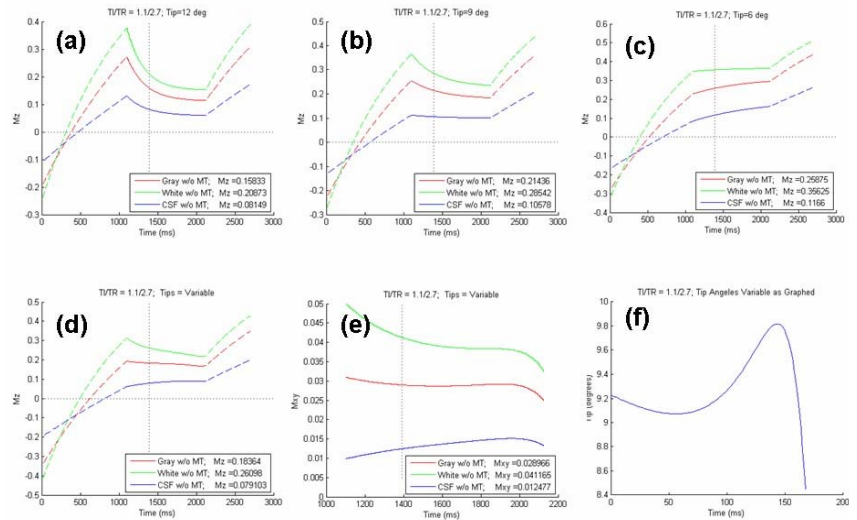


Figure 4: Signal simulations for MPRAGE

practice, however, this solution is difficult to implement because of flip angle errors. Furthermore, performance is compromised because not all tissue types reach simultaneously steady state. A solution without the steady state restriction is therefore highly desirable. We propose to develop a new iterative deblurring method for variable T1-weighted imaging which permits non steady state acquisitions.

### C.3.e. Proposed new iterative deblurring method (Drs. Raj, Zhan, Schuff): Initial results of the new

image deblurring methods from simulations are shown in Figure 5. Starting from an experimental MPRAGE image, shown in the top row left column, we first simulated T1-weighted imaging by computing a series of MRIs with exponentially increasing gray matter intensities, shown in the same row middle column. The images were then blurred, as seen in the top row right column, using a gaussian filter of the form  $PSF = \exp\left[-R_1(x-x_0)\right]^2$ , where

$R_1$  is the longitudinal relaxation rate and  $(x-x_0)^2$  the blurring kernel. We compared three different approaches of deblurring: A) blind deconvolution<sup>(86)</sup>, which makes no assumptions about the blurring function; B) conventional iterative deblurring based on the Lucy-Richardson algorithm (available in Matlab), assuming that the shape but not necessarily the width of the blurring function is approximately known and C) our proposed iterative deblurring approach, in which the blurring value is updated after each iteration by updated T1 values from LS fits of the MPRAGE data at each iteration. Deblurred images are shown in the middle row respectively from left to right in the order of blind deconvolution, conventional

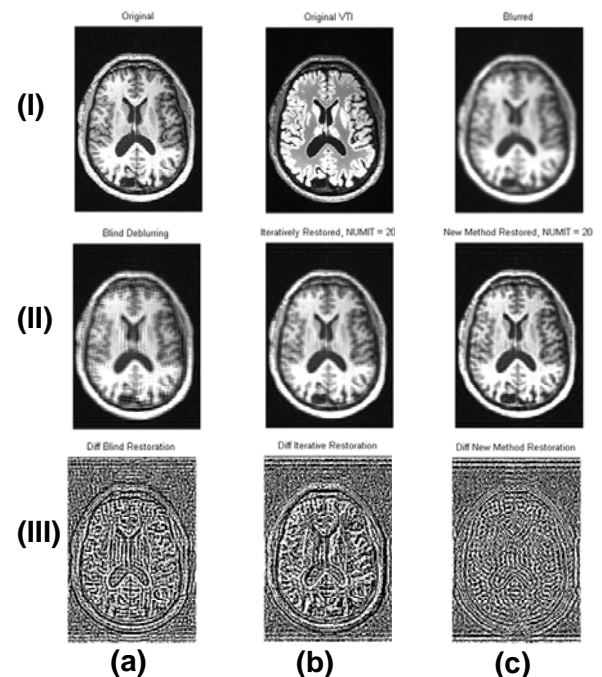


Figure 5: Simulations of image deblurring

iterative deblurring, and the proposed deblurring method. The difference between the deblurred image and the gold standard image is shown for each method in the bottom row in the same order of methods. The proposed deblurring method achieved the smallest difference, i.e. the greatest similarity between deblurred image and gold standard. These results demonstrate the concept of the proposed deblurring method.

#### C.4. Development of ASL Pulse Sequences, Labeling Pulses, and ASL Models:

**C.4.a. Three-dimensional ASL-GRASE:** With support of Dr. Feinberg, we implemented 3D ASL-GRASE at 4 Tesla. Figure 6 depicts a slice from a time series of perfusion images from a healthy volunteer. The acquisition of each 3D ASL frame took less than 34 seconds at a resolution of 4.5 x 4.5 x 4.5 mm up to a total of 10 min for the entire time series with increasing post-labeling delays from 200ms to 2500ms in steps of 100ms. The spatial dispersion in the arrival of the ASL signal can clearly be seen in the upper row of Figure 5. Also clearly visible is the progressive disappearance of the arterial component of the ASL signal, as water diffuses into the brain. The significance of these preliminary data for the proposed work is that it demonstrates the feasibility to acquire serial perfusion images of the whole brain in a few minutes at 4T using 3D ASL GRASE. However, Dr. Feinberg is developing even more efficient acquisitions of 3D GRASE in Project 2 of the Acquisition Core.

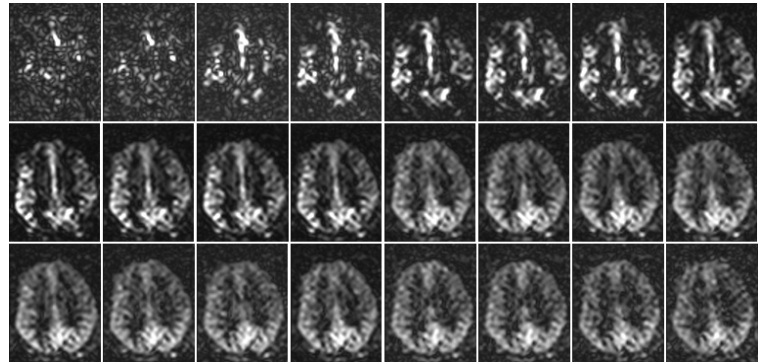


Fig. 6. Perfusion Time Series from 3D ASL-GRASE

**C.4.b. Double Inversions with Proximal Labeling of Both tag and control Images (DIPLOMA):** (see also appendix: A Novel Tagging Method for Multislice Pulsed Arterial Spin Label Perfusion (Geon-Ho Jahng, et al. Magn Reson Med. 2003 Feb;49(2):307-14; see Appendix): Arterial spin labeling often introduces undesirable effects from magnetization transfers (MT) and eddy currents, which can substantially degrade ASL-MRI quality. To reduce both effects, MT and eddy currents, we developed a new ASL pulse scheme, termed DIPLOMA, which is depicted in Fig. 7a for tag (T) and control (C) scans. For comparison, the traditional methods for pulsed ASL, PICORE<sup>(87)</sup> and EPISTAR<sup>(88,89)</sup>, are also shown. An experimental setup of DIPLOMA is shown in Fig 7b. Because both gradients and RF pulses are better balanced in DIPLOMA than in PICORE and EPISTAR, we achieved better MT compensation, as demonstrated on phantoms. Perfusion studies on volunteers, analyzed using first and second order image texture analysis<sup>(90)</sup> showed that DIPLOMA yielded 8% ( $p = 0.003$ ) more signal to noise than EPISTAR and PICORE, 28% ( $p < 0.001$ ) less random variations than PICORE, 23% ( $p < 0.008$ ) higher contrast than EPISTAR and 15% ( $p = 0.006$ ) less angular second moment (better image uniformity) than PICORE. Reliability was also higher for DIPLOMA (0.8 intraclass correlation) than for the two other pALS methods, although the difference was not significant. However, we attempted to further improve pulsed labeling by inventing a new ALS scheme, termed IDOL.

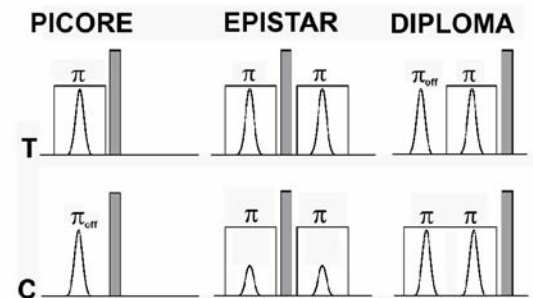
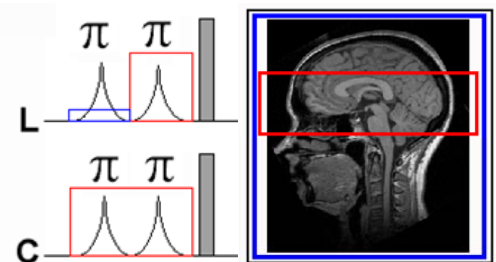


Fig. 7a: Arterial Spin Labeling Schemes



Red/Blue = labeling regions; Black = MRI field-of-View;  $\pi$  = inversion pulse; Gray-colored rectangle = crusher-gradient

Fig.7b: IDOL Labeling

**C.4.c. Modeling of ASL Perfusion:** (see also in appendix: A Four-Phase Single-Capillary Stepwise Model for Kinetics in Arterial Spin Labeling MRI (K-L. Li et al. Magn Reson Med. 2005; 53(3):511-8). We developed an extended model for extracting measures of brain perfusion from pulsed ASL-MRI data with consideration of transit effects and restricted permeability of capillaries to blood water. The time course of the signal difference between control and labeled images was divided into four phases with respect to arrival time of labeled blood water at the voxel of interest ( $t_A$ ), transit time through the arteries in the voxel ( $t_{ex}$ ), and duration of the bolus of labeled spins ( $\tau$ ), as shown in Fig 8. We called this the four-phase-single-capillary-stepwise (FPSCS) model of perfusion. Dividing the labeled slab of blood water into many discrete segments and adapting numerical integration methods allowed convenient modeling of restricted capillary-tissue exchange based on a modified distributed parameter model. A copy of the paper is available in the appendix. An initial set of parametric perfusion maps from a single subject obtained at 4T is shown in Fig. 9. The arrows point to distinct brain regions where we found a large disparity between high CBF and low exchange time. The region of the highest CBF was the posterior cingulate (yellow arrow), also consistent with observations from SPECT and PET. Interestingly, exchange time was generally shorter in frontal than in parietal brain regions. These preliminary data demonstrate our experience with modeling CBF. However, these results were obtained with a 2D sequence and acquisition of ALS-MRI series took 45 minutes. We expect higher sampling efficiency and better sensitivity with serial 3D-ASL GRASE. Furthermore, multi-echo echo acquisitions using 3D-GRASE should improve accuracy to determine the exchange time and water uptake into the brain.

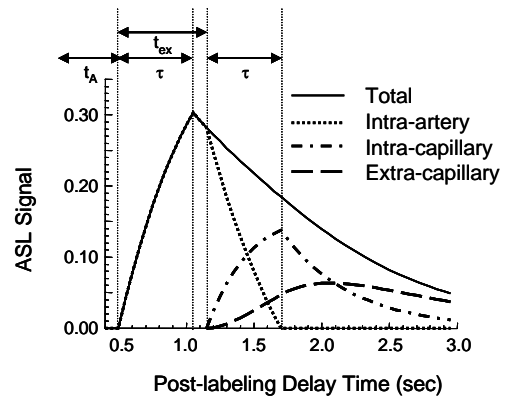
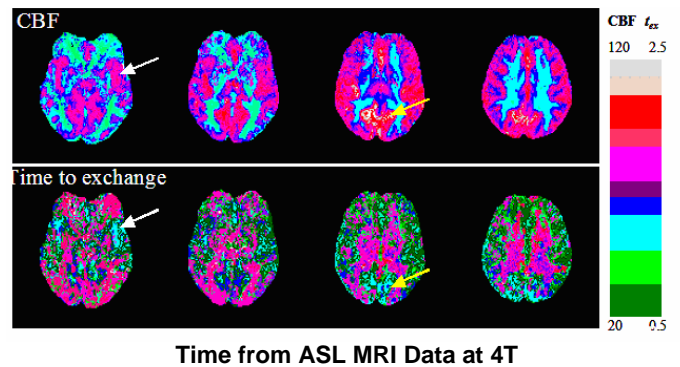


Fig. 8: ASL Signal Modeling



Time from ASL MRI Data at 4T  
Fig. 9: Parametric Maps of CBF and Exchange

**C.4.d. Dynamic ASL perfusion studies in aging and dementia: (Drs. Xiaoping Zhu and Norbert Schuff):** We measured cerebral blood flow (CBF) and arterial transit time (ATT) in 16 cognitive normal elderly, 4 patients with mild cognitive impairments (MCI) and 6 patients with Alzheimer's disease (AD) using pulsed ASL 3D GRASE for acquisition and our four-phase two-compartment perfusion model<sup>(43)</sup> for quantification. We were particularly interested in separating CBF changes, i.e. oxygen demand from ATT changes, i.e. blood supply. Representative CBF and ATT maps from a healthy control and AD patient are depicted in Figure 10, showing substantial CBF loss and ATT prolongation in the patient. A voxel-wise group analysis (SPM2) showed clusters of significant CBF loss and ATT prolongation in parietal-temporal cortices ( $p = 0.001$ ) bilaterally in AD, see Fig 10. Furthermore, CBF was negatively correlated with age ( $R^2 = 0.55$ ,  $p = 0.002$ ), while ATT increased with age ( $R^2 = 0.27$ ,  $p = 0.04$ ). Interestingly, CBF and ATT alterations were significantly correlated in CN and MCI subjects, but uncorrelated in AD, suggesting that different factors govern cerebral blood demand and supply in normal aging and AD. The importance of these results is that accurate measurements of perfusion dynamics, as developed in

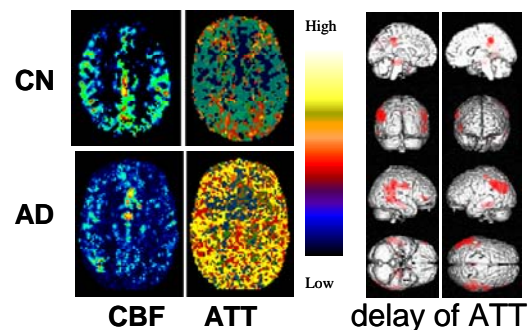


Fig 10. Left: CBF and ATT maps from a 65y cognitive normal (CN) elderly and a 72y AD patient. Right: Statistical parametric maps (SPM) of regional ATT prolongation in AD compared to CN.

this project, could lead to a better understanding of physiological effects that underpin neurodegeneration.

**C.4.e. Effect of parallel imaging on perfusion mapping using ASL-GRASE: (Drs. Zhu, Ji, Schuff):** We assessed the effect of parallel imaging for accelerate measurements of dynamic ASL perfusion and to reduce susceptibility distortions in ASL 3D GRASE. We used an 8 channel head coil and GRAPPA parallel image reconstruction for dynamic ASL perfusion acquisitions (13 time series frames, each 22 slices) on five volunteers. We tested 3 different approaches for image reconstruction: 1) full reconstruction of all datasets without parallel imaging, as the gold standard; 2) GRAPPA reconstruction with use of 16 reference lines for each time series dataset, termed GRAPPA(I), yielding an affective acceleration by a factor 1.5 and 3) GRAPPA reconstruction with use of 16 reference lines for only one representative dataset of the time series (the middle one) as calibration for the reconstruction of the rest of the frames, termed GRAPPA(II). We found that GRAPPA (II) with only one time calibration, though very efficient in sampling, degraded CBF quantification. In contrast, GRAPPA (I), though less efficient in sampling, provided results comparable to those obtained with the gold standard. Figure 11 shows results of parametric estimations of blood flow (CBF, left column) and arterial transit time (ATT, right column) using the gold standard (top row), GRAPPA(I) (middle row), and GRAPPA(II). The red arrows indicate, where substantial differences between the gold standard and GRAPPA (II) or GRAPPA (I) were observed. These preliminary results demonstrate that dynamic perfusion imaging with 3D GRASE and acceleration by parallel imaging is feasible.

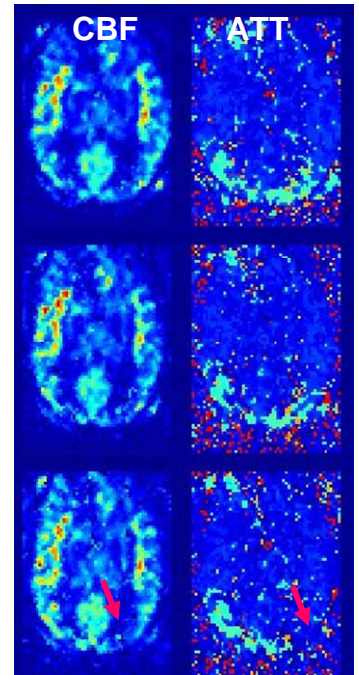


Figure 11: Parametric maps of blood flow (left) and arterial transit time (ATT) obtained using GRAPPA (I) (middle row) or GRAPPA (II) (bottom row), compared to the Gold Standard (top row).

**C.4.f. Effect of  $T_2^*$  on cerebral blood flow quantification using serial multi-echo ASL 3D GRASE (Dr. Zhu):** Previous ASL models of perfusion included longitudinal relaxation ( $T_1$ ) differences between blood and tissue water<sup>(51)</sup>, while transverse relaxation,  $T_2/T_2^*$ , has usually been ignored. Neglecting  $T_2/T_2^*$  effects can lead to errors in estimating perfusion when  $T_2/T_2^*$  of water in tissue is substantially different from that in arterial blood (venous outflow is usually negligible for ASL). We aimed to evaluate effect of  $T_2$  on CBF estimations. We measured the post-labeling evolution of the ASL signal, including  $T_2$  variations, using dynamic ASL- 3D GRASE with interleaved dual echo acquisition. CBF was estimated using the four phase dual compartment perfusion model, termed FPSCS and introduced in ref<sup>(43)</sup>. For this application, we expanded FPSCS to account for differences in  $T_2$  between tissue and blood, termed FPSCS $_{T_2^*}$ . Dynamic ASL 3D GRASE series consisting of 20 frames for different inversion times (from 300-3300 ms) and interleaved echo acquisitions with  $TE = 37.5, 75.0$  and  $112.5$  ms were acquired on 3 volunteers at 4T. The acquisition time per frame was about 24 seconds and the total scan time was less than 5 min with the adaptive TR and a fixed echo time. At present, fixed parameters for  $T_2$  of arterial blood ( $T_{2a} = 70$  ms) and brain tissue ( $T_{2t} = 40$  ms) were used to fit the dynamic perfusion signal, yielding parametric maps for CBF and arterial transit time (ATT). Histograms of CBF estimations without (FPSCS) and with (FPSCS $_{T_2^*}$ ) consideration of  $T_2$  are shown in Figure 12A. This demonstrates that ignoring  $T_2$  leads to an underestimation of CBF. Furthermore,  $T_2$

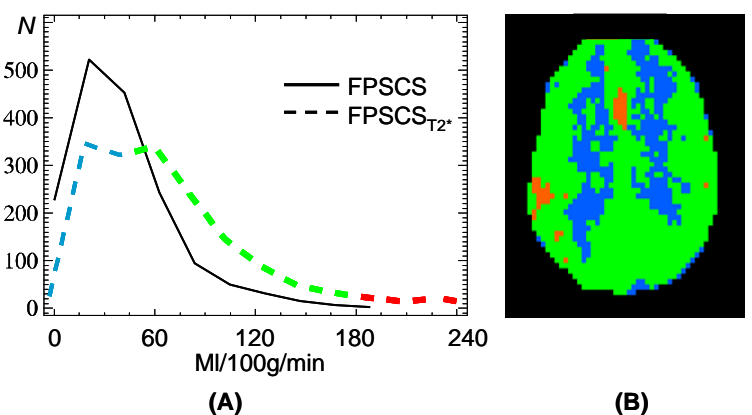


Figure 12:  $T_2^*$  effects

**inclusion yields a bimodal CBF distribution, in contrast to absent T2 effects. Segmented CBF maps of low (blue), median (green) and high (red) perfusion values based on the bimodal histogram are shown in Figure 12B. These results indicate the value of measuring T2 in ASL to quantify perfusion. The T2 information from ASL spins could also potentially be useful for measuring blood brain barrier permeability of water.**

**C.4.g. Prototype of an Easy-to-Use ASL-Toolkit for ASL Processing:** We have developed prototype ASL-toolkit software based on MATLAB code for quantification of multislice CBF maps pulsed ASL or amplitude-modulated continuous ASL imaging data, acquired at a single postlabeling delay time. In the toolkit, time series raw data are realigned and resliced to compensate for head motion between acquisitions. Resliced labeled and unlabeled images are then pair-wise subtracted from each other to obtain perfusion weighted images. For CBF quantification, tissue T1 maps are calculated from EPI data using a two-point inversion recovery method developed in this lab<sup>(91)</sup>. Currently, the CBF quantification is based on a single-compartment model, assuming instantaneous mixing of ASL water between capillaries and brain tissue. The model takes also into account the initial magnetization of blood and blood-tissue partition coefficients ( $\lambda$ ) of gray matter and white matter using information from segmented high resolution of 3D T1-weighted image, coregistered to the perfusion images. Measured labeling efficiency ( $\alpha$ ) is also used in the model. T1 values of blood taken from literature ex-vivo data. After CBF maps are calculated, the toolkit permits easy visualization and assessment of quality of the perfusion data and further use for voxel-wise analysis, e.g. with SPM.

## D. RESEARCH DESIGN AND METHODS

**D.1. Development of VTI:** This section describes the work plan to accomplish specific Aim 1, i.e. the development of multi-acquisition variable T1-weighted imaging (VTI) for resolving voxel compartmentation and enhancing resolution. The phases of development will include simulations, phantom studies, and validation tests. Finally, VTI will be applied to clinical studies. In the first year of funding, we will also collect preliminary VTI data using best guess parameter settings to provide the Processing Core with preliminary data for development of segmentation methods that utilize the features of VTI.

**D.1.a. Conceptual design:** Our goal is to seek a set of acquisition parameters which yield the highest precision across a large T1 range to estimate subvoxels with two or three compartments, while keeping acquisition time at a minimum (our target is the acquisition of 12-20 VTI frames in less than 30 min). The acquisition methods, which we will consider for VTI include: 1) FLASH imaging with variable and flip angles and shortest repetition time (TR); 2) FLASH with variable TR and fixed flip angle, and 3) MPRAGE imaging with variable inversion-recovery times but fixed TR. Simulations will be performed to study the influence of flip angle errors, noise, and spatial misregistrations on accuracy and precision. We will simulate the steady-state signal in FLASH and MPRAGE under the condition of multiple compartments in an image voxel with a linear superposition of the signal from the different subvoxel compartments according to

$$S \propto \sum_{n=1}^N \beta_n f \left( e^{-tR_1^{(n)}} \right) + \text{bias}(\beta_1, \dots, \beta_{m \notin n}),$$

where  $f$  is a function which depends on the sequence.  $n$  runs over all tissue components, i.e. gray matter, white matter, CSF,  $\beta_n$  are weights of the signal from the different compartments with the condition

$$\sum_{n=1}^N \beta_n = 1$$

and  $R_1^{(n)}$  is the characteristic relaxation rates of each compartment. The ultimate objective is to estimate the weights  $\beta_n$  from a series of VTI frames. The bias term  $\text{bias}(\beta_1, \dots, \beta_{m \notin n})$  is the signal component from spurious contributions of other tissue types, such as white matter lesions or blood vessels. The bias term is, by hypothesis, a function of the weights  $\beta_n$ , since the higher their sum for a voxel the less likely are spurious contributions to the signal from other tissue types. The bias term will allow us to differentiate between systematic and random errors. **Our preliminary results suggest that we can obtain stable LS fits with 3**

degrees of freedom (DoF), i.e. one degree for T1 and water density, respectively and another degree for flip angle errors. We expect that an inclusion of spatial priors for LS fits will provide stable solutions of the inverse problem for one more DoF, i.e. for the bias term. With at least four DoFs, we will be able to model a dual compartment voxel with variable gray and white matter contributions in a voxel as well as for a variable flip angle.

**D.1.b. Development of T1 estimations by least-squares (LS):** Our preliminary results shown in C.3.c indicate that the inclusion of a simple spatial prior with quadratic smoothness (known as the 1<sup>st</sup> order Tikhonov regularization) stabilized the fits and yielded improved T1 estimations. We plan to extend this approach to 3D in order to impose stronger spatial priors. However, smoothness priors are not desirable for high resolution MRI. We will therefore develop methods to allow using even more powerful spatial priors with edge-preserving characteristics of the form discussed in the Reconstruction Core, project 3 (PI Raj). In addition, we propose to vary both the flip angle and pulse spacing to achieve greater signal diversity, as described in D.1.c below. We expect the methods allow attaining stable solutions with one more degree of freedom to account for spurious tissue contributions, i.e. the bias term  $bias(\beta_1, \dots, \beta_{m \in n})$ .

**D.1.c. A new multiple acquisition method for subvoxel quantitative T1 measurements using optimal data diversity (Dr. Raj):** Recall that the single compartment signal equation for FLASH imaging is given by

$$M(T_1, \rho_0, \alpha) = \rho_0 \exp(-te/T_2) \sin \alpha \frac{1 - \exp(-\tau/T_1)}{1 - \cos \alpha \exp(-\tau/T_1)}.$$

Here,  $\rho_0$  is the spin density,  $te$  the spin echo time, and  $\tau$  the spacing of the RF pulses with flip angle  $\alpha$ . Now, since  $\tau \ll T_1$ , we have  $\exp(-\tau/T_1) \rightarrow 1 - \tau/T_1$ . Therefore we have

$$M(T_1, \rho_0, \alpha) = \rho_0 \exp(-te/T_2) \sin \alpha \frac{\tau/T_1}{1 - \cos \alpha + \cos \alpha \cdot \tau/T_1}.$$

We propose to vary BOTH  $\alpha$  as well as  $\tau$ , in order to achieve a better signal diversity which will allow us to optimally estimate  $T_1$ . Note that this is different from our original proposal where we proposed to vary only alpha. We believe that varying both these parameters is likely to produce greater signal diversity which is very important for any inverse problem, especially the least squares fit described later. The introduction of  $\tau$  as a variable parameter also allows us to circumvent to some extent the problem of spatially ambiguous flip angle, due to which the exact flip angle at any point in the image might not be the same as the nominal flip angle. However, we note that for practical (SNR and acquisition time) reasons, we wish to limit both  $\alpha$  and  $\tau$  to small values. Consider two representative cases:

- When  $\alpha \ll 1$ ,  $M(T_1, \rho_0, \alpha) \approx \rho' \sin \alpha$

This situation is great for estimating spin density (but not T1, since there is no dependency on T1). However, due to lack of sensitivity w.r.t.  $\tau$ , there is no point varying  $\tau$  in this regime.

- When  $\alpha = 60$  degrees,  $M(T_1, \rho_0, \alpha) = 2\rho' \sin \alpha \frac{\tau/T_1}{1 + \tau/T_1}$

This situation of higher  $\alpha$  is therefore good for estimating  $T_1$ , which is now sensitive to both  $\alpha$  and  $\tau$ . The above argument suggests a sensible scheme for estimating  $\rho_0$  and T1 jointly, by repeated experiments with varying  $\alpha$  and  $\tau$  as per the following table:

	TR = 5 ms	TR = 10 ms	TR = 20 ms	TR = 40 ms
$\alpha = 10$	X			
$\alpha = 20$	X	X		
$\alpha = 30$	X	X	X	
$\alpha = 40$	X	X	X	X

We propose to employ this experiment design to obtain a set of values of M for each voxel. We estimate that about 10% diversity can be gained with this method at 4T, given the tissue T1 values and  $\tau$  up to 40ms. Then we will find an initial solution of  $\rho_0$  and T1 by a least squares fit, independently for each voxel. We expect that due to poor SNR of the imaging experiments, exacerbated by our use of higher than optimal  $\alpha$ , the LS fit might not produce a high quality accurate  $\rho_0$  and T1 maps. To improve the situation further, we will employ a new Bayesian estimation technique, which will introduce spatial priors to overcome noise in estimation.

**D.1.d. A new deblurring method for variable T1-weighted imaging (Drs. Raj, Zhan, Schuff):** Recall that in MPRAGE, the magnetization is not continuously in steady-state free precession (SSFP) because the progression towards steady-state in the inner loop (1<sup>st</sup> phase encoding) of MPRAGE is disturbed by an inversion time (TI) and recovery delay (TD) in the outer loop (2<sup>nd</sup> phase encoding). Spatially encoding transient magnetization on its way to SSFP will cause image blurring. Blurring is minimized in conventional MPRAGE by delaying the sampling of the central part of k-space until the magnetization reaches steady state or by varying the flip angle during the RF pulse train. However, this can lead to SNR and contrast losses<sup>(17)</sup>. Although several enhancements to MPRAGE have been proposed to deal with blurring, including centric sampling<sup>(17)</sup> and interleaved squared-spiral phase-encoding<sup>(92)</sup>, these methods are suboptimal for simultaneously maximizing contrast/SNR and minimizing blurring.

We propose to develop a novel iterative deconvolution method that deals with blurring in variable T1-weighted MPRAGE. Recall that for a sequence of  $n$  infinitely short and rapid  $\alpha$ -pulses with a pulse spacing  $\tau$ , the signal  $S_n$ , having an initial magnetization  $M_0$  and a longitudinal relaxation rate  $R_1$ , evolves during the pulse train according to<sup>(93)</sup>:

$$S_n \propto \left( M_0 \cdot \cos^{n-1} \alpha \cdot e^{-n\tau R_1} + C_n \right) \cdot \sin \alpha,$$

with

$$C_n = \left\{ \begin{array}{l} M_{eq} \left( 1 - e^{-\tau R_1} \right), \text{ for } \dots n = 1 \\ C_{(n-1)} \cdot e^{-(n-1)\tau R_1} \cos \alpha + M_{eq} \left( 1 - e^{-(n-1)\tau R_1} \right), \text{ for } \dots n > 1 \end{array} \right\}.$$

Here, the index  $n$  is equivalent to the  $n$ 'th phase encoding step in the inner loop of MPRAGE. Furthermore,  $M_0(TI) = \left( 1 - 2e^{-TI R_1} \right)$  for MPRAGE with inversion time TI. It is easy to see that the first term in  $S_n$  reflects the decay of  $M_0(TI)$  and the second term  $C_n$  signal recovery from equilibrium  $M_{eq}$ . Together, they describe a transient signal on its way to steady state that may cause image blurring. Note also that  $C_n$  is independent from  $M_0(TI)$ . The blurring values can be estimated, and thus deblurring applied, if  $R_1, M_0, \alpha$  and  $M_{eq}$  are known. While  $R_1, M_0$  and  $\alpha$  can be measured,  $M_{eq}$  is usually not known. However, the effect of  $M_{eq}$  can in principle be eliminated by collecting two MPRAGE sets A and B with different values for TI such that  $M_0^{(A)} = -M_0^{(B)}$  and subtracting  $S_n^{(B)}$  from  $S_n^{(A)}$  for each  $n$ .

The discourse above provides a strategy for deblurring of MPRAGE. After reconstruction of MPRAGE images that might be blurred, initial estimates of  $R_1, M_0$  are obtained by LS fits of the data as described in D.1.b. The effective flip angle  $\alpha$  can be experimentally determined<sup>(18)</sup>. The estimates of  $R_1$

and  $M_0$  together with  $\alpha$  are used as to obtain an initial estimate of the blurring value (or PSF) of MPRAGE. The MPRAGE images are then deconvolved and new  $R_1$  and  $M_0$  estimates are obtained, which are then used in turn to re-estimate new blurring values and so on. We expect that our method will perform better than blind deconvolution, because we can use a parametric form of the blurring function, i.e. using Dr. Matson MatMRI simulations proposed in Project 3 of the Acquisition Core. We expect that our method also performs better than conventional iterative deblurring methods, because we update the parameters of deblurring after each run in contrast to conventional iterative methods, which only rely on initial estimations. A sketch of the iterative procedure is shown in Figure 13. We will initially establish deconvolution for 1D, i.e. the inner phase-encoding loop of MPRAGE and then expand the solution to 2D by allowing the inner loop of MPRAGE to step simultaneously through both directions, i.e. along squared spirals<sup>(92)</sup> or a 2D centric array. The extension to 2D may raise complications, if the two-dimensional PSF is not reducible, in which case convergence may not be guaranteed. We plan to impose convergence by restricting 2D sampling to patterns with rotationally invariant blurring functions. In this regard, 2D spiral phase-encoding, which yields approximately a circular PSF, might be better than centric encoding, which yields a PSF that stretches along the cardinal directions. We will start with the conventional expectation maximization (EM) algorithm for image deblurring, also known as the Richardson-Lucy algorithm<sup>(94)</sup>. Although convergence of the EM algorithm for conventional deconvolution is well established<sup>(95)</sup>, our iterative approach to update the blurring function may interfere with convergence. We plan to extend the EM approach by allowing priors, similar to those discussed in D.1.b., in order to minimize total variation in the image and the PSF expressed as regularization, in addition to minimizing the mean square error between the observed and original data.

**Stopping criteria:** Since the inverse problem is ill-posed due to presence of noise, the iterations may lead to exaggerated edges and noise. We will initially define an edge-noise-ratio to balance the edge improvement and the noise effect. The optimal balance will be established on a resolution phantom. However, this approach requires identification of edges in the images. Dr. Thayyullathil of our lab has developed an effective edge detection algorithm. However, the procedure may perform suboptimal in regions with a low contrast where edge detection is difficult. Furthermore, finding the optimal edge-noise-ratio balance for in-vivo data may be difficult because of the large degrees of freedom. We therefore plan to develop better stable stopping criteria. A new promising stopping criterion is the scaled entropy of the cooccurrence statistics of an image. Dr. Hadjidemetriou of our lab has recently implemented this approach as stopping criterion for iterative restorations of MRI from B1-field Inhomogeneity<sup>(96)</sup>. Since the deblurred image is the one whose cooccurrence matrix has minimum scaled entropy, we plan to use the scaled entropy as stopping condition for iterations.

**D.1.e. Simulations:** We will use first order error propagation theory, assuming initially a noise free signal, to drive the selection process for the optimal FLASH or MPRAGE parameters that provide precise estimates of the weights  $\beta_n$ . We will then extent the analysis to a noisy signal using Monte-Carlo simulations. Both Gaussian and Rician noise patterns will be considered and bias on estimating the weights from VTI data in the presence of poor signal-to-noise investigated. We will further evaluate the effect of image misregistration on subvoxel estimation by imposing spatial variations on the weights Our goal is to seek a set of acquisition parameters which yield the highest precision across a large T1 range to estimate subvoxels with two or three compartments, while keeping acquisition time at a minimum (our target).

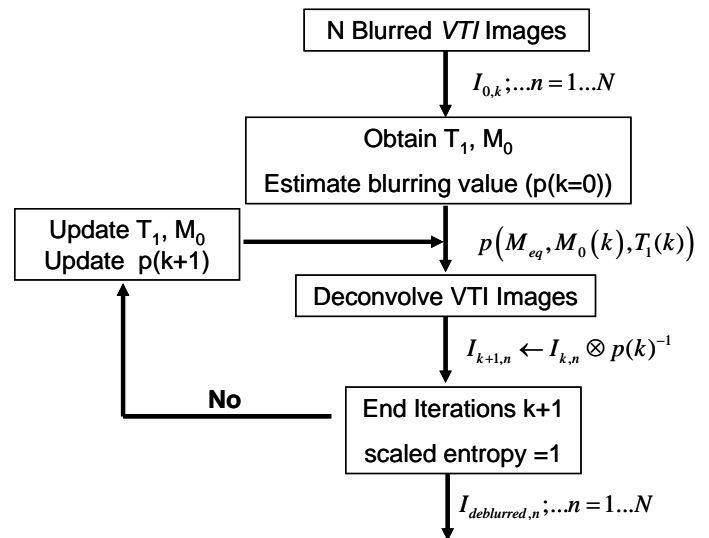


Figure 13: Diagram for iterative deblurring

## D.1.f. Validation

**D.1.f.i. Phantom Studies:** The goal of phantom studies is to test and minimize systematic differences between VTI and a high-resolution gold standard study. Quantitative studies will be performed using the ADNI phantom, which contains a large set of small water filled spheres in a doped water bath as well as four larger spheres with different T1 values. The ability of VTI to accurately predict partial volumes will be compared to “gold standard” very high-resolution acquisitions. Image segmentation will be used as a metric for the comparison. Systematic flip angle offsets will be introduced to study the effect of RF pulse imperfections on T1 estimations. Moreover, the B1-insensitive RF pulses developed by Dr. Matson will be used and evaluated in conjunction with VTI. We will also evaluate spin-echo EPI sequences for rapid B1 mapping, such as the variable RF-pulse duration approach by Ordidge et al <sup>(97)</sup> to determine regional flip angle variations. The potential for noise bias will be studied by reducing slice thickness and increasing the acceleration factor in parallel imaging. Image misregistration will be studied by introducing voxel shifts when reconstructing complex image data.

For studies that require high precision in resolution, such as deblurring tests and comparisons between VTI and high resolution MRI, we will use the well-known “star-wedge” phantom shown in Figure 14. The phantom is designed to provide measurements of spatial resolution on a quasi continuous scale.

The smallest resolvable distance  $dx$  can be determined from the radius  $R$  of the inner circular area that remains unresolved in the image, according to:

$$dx = (R - d) * 2 \tan(\alpha/2) * \sin \phi \approx (R - d) * 0.105 * \sin \phi$$

where,  $d$  is the thickness of the plastic rods,  $\alpha$  the angle between rods, and  $\phi$  is the tilt between image plane and the plastic rods, which should be  $\phi \approx 90$  ( $\rightarrow \sin \phi \approx 1.0$ ) to make measurements simpler. We have built a star-wedge phantom with dimensions that allow resolving a minimum of 2 mm in R and hence about 0.2 mm variations in MRI resolution. This phantom should provide very sensitive measurements for tests of deblurring and for comparisons between VTI and high resolution MRI.

**D.1.f.ii. Validation using in-vivo data:** For in-vivo validation, we will perform back-to-back studies and cross-sectional studies of a small group (N=10) of controls and patients. Back-to-back studies will be used to determine reproducibility, i.e. expressed as intraclass coefficient. The cross-sectional studies will be used to determine the effect size, i.e. difference of the means divided by the pooled variance of the groups in separating controls from patients. Increased reproducibility and effect size will be used to determine improvement.

**D.1.f.iii. Comparisons between VTI and high resolution MRI:** In order to compare the accuracy of tissue characterization using the subvoxel method and high resolution imaging for the same scan time, we will scan a total of 15 subjects in 3 groups, 5 young and 5 older controls, and 5 patients with MCI using both methods. Each subject will be scanned back-to-back using both VTI and high-resolution MPRAGE. The targeted resolution of the high-resolution MPRAGE will be about  $0.7 \times 0.7 \times 0.7 \text{ mm}^3$ , which will require a roughly 9 times longer acquisition time than a VTI frame for equivalent SNR values. Both acquisitions will be optimized for high contrast to noise, based on extensive simulations using Dr. Matson’s MatMRI program and on the optimized deblurring methods, developed in this project. Processing of the data will be performed using improved methods for bias field correction and segmentation, which are developed in the Processing core respectively by Dr. Hadjidemetriou and Dr. Zabih. We will use effect size, defined as group difference between the means divided by the pooled group variances, as statistical metric for quantitative comparisons between the two MRI acquisition methods. Based on the well establish finding that both aging and MCI are associated with cortical atrophy we will compare the effect size to which each method separates young from older subjects and healthy subjects from MCI patients. Furthermore, to determine if the differences between effect

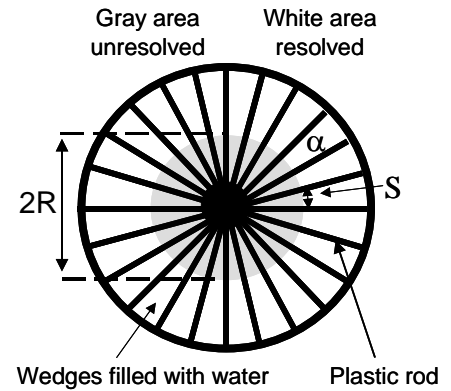


Figure 14: Phantom

sizes are statistically significant, we will perform logistic regressions as measure of power of each MRI method to correctly classify each group and leave-one out cross-validations to obtain the distributions of sensitivity and specificity of each method, expressed as areas under the curves (AUC) from an receiver operator characteristics analyses. Mann-Whitney tests will then be used to compare the AUCs.<sup>23</sup> The significance level will be  $\alpha < 0.05$  for all tests.

**D.2. Development of quantitative evaluations of CBF and water uptake:** This sub-section describes the work plan to accomplish specific Aim 2, i.e. the quantitative evaluations of cerebral blood flow and water uptake into the brain, distortion corrections of 3D-GRASE and development of a user-friendly software package for processing and evaluating ASL-MRI data.

**D.2.a. Modeling of CBF and water uptake:** We will build on our previous work<sup>(43)</sup> to improve dual-compartment distributed-parameter models for perfusion by considering the advantages from volumetric acquisitions of 3D ASL-GRASE. A regular simplex fitting algorithm may no longer handle all model parameters and solutions may become unstable. We will therefore explore a maximum a posteriori algorithm, which imposes conformity with the two compartment model and may help to stabilize the situation. In our current version of a perfusion model, we account for variable arterial transit times (ATT), bolus dispersion ( $\tau$ ), a time lag ( $t_{ex}$ ) for blood in arterioles progressing towards the capillary bed, T1 relaxation of blood and brain tissue, and finite rate of water uptake into brain. We further account for a distributed concentration of spin labels along capillaries. We can largely condense calculations by transforming the temporal-spatial dependency of the perfusion signal into a temporal dependency alone, which has the advantage that fitting algorithms can use small, consecutive time segments. From the mass balance of labeled blood water, we can then derive differential equations of the labeled water concentration in intra- and extra vascular space for each time segment. To simulate distributed tracer concentrations, we will use a sliding segment algorithm with serial loops of discrete events. This approach will also be convenient to model multi-echo acquisition of 3D ASL-GRASE and variations of the transverse relaxation of the ALS signal from exchange between intra and extra-vascular space. We will implement the algorithm on our 24 node Beowulf parallel computer architecture to achieve maximal processing speed. We will further perform Monte-Carlo simulations to study the stability of the algorithm to variations in the kinetic parameters and potentially reduce the number of variables. Furthermore, we will explore bias in estimating CBF and water exchange as a function of SNR.

**D.2.b. Quantification of transverse relaxation of labeled spins.** Multiple-echo 3D ASL-GRASE offers a possibility to measure variations of the transverse relaxation of the ASL signal, which could be extremely valuable for studies of the dynamics of water uptake into the brain. Figure 15 shows one implementation of multi-echo ASL 3D GRASE. After spin labeling and an inflow delay (TI), the first sequence of 3D GRASE, termed Echo 1, maps perfusion starting at  $t = TE$  after the excitation pulse. Another sequence, termed Echo 2, maps perfusion starting at  $t = (1+n) \cdot TE$ , where n is the number of 180-180 blocks after the excitation pulse. T2 information of the ASL signal as a function of post-labeling delay can be obtained from the ratio of Echo 1 and Echo 2. Note, an additional degree of freedom needs to be added to account for variations of the initial magnetization, because these are interleaved and not dual echo acquisitions. Dr. Feinberg will develop improved and more efficient multiple echo ASL 3D GRASE sequences in project 2 of this core.

We will expand our four phase single capillary stepwise (FPSCS) model published in<sup>(43)</sup> by considering effects on the ASL signal due transverse relaxation. Initially, we will include T2 effects in

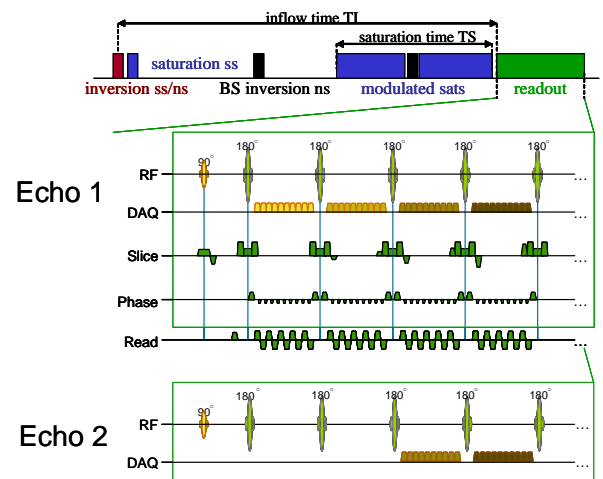


Figure 15: Interleaved echo acquisition in ASL 3D GRASE

the FPSCS model assuming a homogenous distribution of T2, i.e. instantaneous exchange of water between capillaries and the brain. We will then relax the condition of a homogenous distribution of T2 by assuming a finite rate of exchange for water between capillaries and the brain, which can lead to modulation of the apparent T2 as a function of post-labeling delay. Since the addition of T2 will increase the degrees of freedom for fitting the perfusion by at least 2 (one degree for T2 and another for variable initial magnetization because acquisitions are interleaved), we will carefully investigate error propagation and stability of the fits using Monte-Carlo simulations. There are several solutions to stabilize the ASL fits: 1) noise reduction using principle components analysis, similar to the algorithm we developed for denoising MR spectroscopy, published in reference <sup>(98)</sup>. 2) Joint analysis of perfusion T2 and T1 fits and 3) development of algorithms that allow including spatial priors for fits of perfusion.

In addition to T2, we will also develop models to analyze T2\* obtained with multi-echo ASL-GRASE. This has potential value for joint functional ASL and BOLD studies in ND. Dr. In project 2 of this core, Dr. Feinberg will develop modifications of 3D ASL-GRASE to achieve measurements of T2\*.

**D.2.c. Validation:** CBF measurements from 3D ASL-GRASE will be validated in-vivo on healthy volunteers by using established experimental techniques for fMRI, such as keeping eyes open or closed and performing demanding cognitive tasks, i.e. recognizing correct arithmetic of numbers displayed on a computer screen. Specifically, a session will consist of four 3D ASL-GRASE measurements of blood flow; three baseline scans (i.e. eyes open or closed) and a third scan during performance of a demanding cognitive tasks over about 15 min. At baseline, CBF will be measured at "resting state" (eyes closed) twice to determine reproducibility of 3D ASL-GRASE and a third time during a simple activation (eyes open) while the subject is lying still in the magnet. At the fourth scan, CBF will be measured while the subject is performing a demanding cognitive task over a long period. Global and regional CBF values will be determined and compared with literature value from similar studies by H<sub>2</sub><sup>15</sup>O PET <sup>(100)</sup>. We plan to enroll 10-20 subjects for this test. The analyses will be performed in normalized space coordinates within the framework of Statistical Parametric Mapping <sup>(101)</sup>.

**D.2.d. In-vivo Studies:** We will collect and analyze serial 3D-ASL GRASE data from healthy subjects and patients with neurodegenerative diseases, including Alzheimer's disease, Parkinson's disease, Amyotrophic Lateral sclerosis and other neurodegenerative diseases. These studies will be performed in conjunction with the collaborative projects of the Center. We will study a subset of controls and patients with both single and multi-echo 3D-ASL GRASE to determine the value of multiecho acquisitions and the feasibility to detect systematic differences between groups in water uptake into the brain. Performance comparisons of ASL-MRI methods will be evaluated by means of quantifiable measures, such as image texture analysis <sup>(90,102)</sup>, reliability and reproducibility, and effect sizes (difference of group means / pool standard deviations). To determine precision (systematic errors) and reliability (random errors), we will study volunteers twice to allow separating between subjects from within-subject effects and noise based on linear mixed effects models.

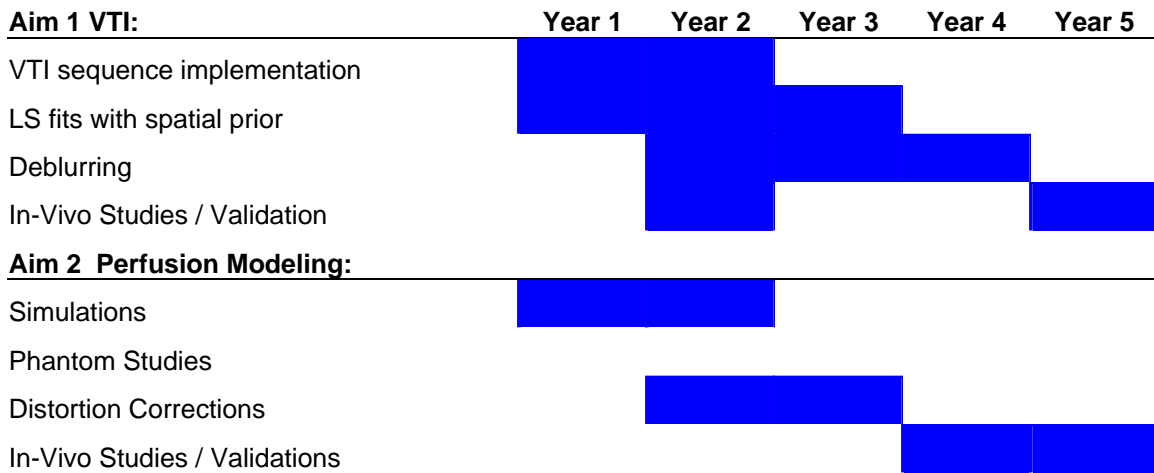
**D.2.e. Distortion Correction by Dynamic Time Warping (DTW):** We will explore the use of DTW to correct 3D-GRASE data for geometrical and intensity distortions from magnetic background gradients. We will first implement DTW, as outlined in Ref <sup>(76)</sup>. We will test the algorithm by simulations of GRASE sets under the influence of an imposed inhomogeneous field using a spin based simulation package and an experimental 2D GRASE image as object. We will do this using complex GRASE data sets to simulate phase twist and wrap. Two images with opposite readout directions will be simulated. To evaluate DTW, the final processed images will be compared to the original pristine image via subtraction of the latter from the former. We will further investigate robustness of DTW as a function of EPI length (= extent of phase error accumulation) and SNR of the images. We will also explore the effect of constraints, such as restricting the direction of the path through the DTW matrix to improve performance and speed. We will further compare DTW results with those from a conjugate gradient algorithm. Real experiments will be performed using a water-filled phantom with glass tubes containing water with different gadolinium doping and air. Tests involving in-vivo data will be performed using 3D ASL-GRASE data sets that were acquired for CBF validation.

**D.2.f. Development of a User-friendly ASL-ToolKit:** The developments of a user-friendly ASL-toolkit software package will focus on three major issues: First, a toolkit will be developed to handle serial 3D ASL GRASE data, as developed by Dr. Feinberg in Project 2 of the Acquisition Core. The toolkit will incorporate

image registration of individual image frames to correct for head movement between frames and registration with anatomical MRI data for anatomical reference. Furthermore, the toolkit will incorporate DTW capabilities for geometrical and distortion corrections. Furthermore, the toolkit will incorporate estimations of arterial transit times and brain T1 information from VTI data sets for CBF quantification. Second, the toolkit will be developed to allow easy integration of the 3D ASL-GRASE data with statistical parametric mapping software (SPM) software. This involves spatial normalization of 3D ASL-GRASE data to template brains and brain atlases. Furthermore, the toolkit will incorporate procedures for atrophy and partial volume correction of CBF using information from tissue segmented high resolution VTI data sets co-registered with 3D-ASL GRASE. Third we will incorporate in the ASL-toolkit the functionality for CBF quantification based on the four-phase-single-capillary-stepwise (FPSCS) model to estimate CBF and water uptake into the brain <sup>(43)</sup>. Currently, the toolkit has implemented only a single compartment model, ignoring non-uniform distributions of labeled water in the capillary bed and finite rates of exchange between intra and extravascular spaces. The fully developed toolkit will further provide estimations of cerebral blood volume (CBV) based on estimations from the FPSCS model of the vascular component of the ASL signal. The toolkit will provide a graphical user interface for easy use. It will also use standard formats for representing data and graphics for easy integration into common statistical analysis programs, such as Statistical Parametric Mapping (SPM, Wellcome Department of Imaging Neuroscience, London), FSL (University of Oxford, UK), and the statistical computing and graphics program R (<http://www.r-project.org/>). The toolkit will be developed in the MATLAB software environment, allowing easy expansion and integration into other MATLAB applications.

**D.3. Software Availability:** To facilitate the application and testing of the proposed imaging methods, we will develop efficient algorithms and computer software implementing the imaging methods developed in this project. We will release the software for public use so that other research groups can evaluate the methods as well. We will further expand our software system with advanced algorithms for image reconstruction capabilities and modeling perfusion dynamics. We will also upgrade the website for the software system to improve communications among the users so that their feedback and comments will be addressed and incorporated in our research when appropriate.

**D.4. Timeline of the Work Plan**



**D.5. Interactions with other Projects**

**D.5.a. Interactions with other TRD projects:** This project will mainly interact with Dr. Matson’s MRI simulation project and Dr. Feinberg’s perfusion project, both in the Acquisition Core, as well as with Dr. Raj’s project on parallel imaging in the Reconstruction Core, Dr. Studholme’s project on building a T1 brain atlas and Dr. Sahib’s segmentation project, both in the Image Processing Core.

The interactions with Dr. Matson’s projects will primarily concern optimization of acquisition parameters for FLASH and MPRAGE with variable flip angle and TI timing. The interactions with Dr. Feinberg’s project will primarily concern improved sampling of dynamic perfusion using 3D ASL

**GRASE sequence for improved quantification of CBF and transit times of perfusion labels.** The interactions with Dr. Raj's project is fundamental to the development of VTI. The ability to obtain multiple scans with variable T1-weighting in a practical scan time will dependent to a large extent on the acceleration factors that Dr. Raj can achieve for parallel imaging. The interactions with Dr. Studholme's project will mainly concern the accuracy to obtain T1 and water density maps to atlases for T1 and water density norms related to aging and neurodegenerative diseases. The interaction with Dr. Sahib's project will primarily concern improvement for segmentation. It is expected that the VTI method allowing subvoxel classification will markedly improve tissue segmentation by resolving ambiguous situations in image contrasts due to partial volume effects and by providing additional input channels (T1 and rho) for multispectral segmentation.

**D.5.b. Interactions with collaborative projects:**

This project will also have tight interactions with several collaborative projects, including the Epilepsy study by Dr. Laxer, the FTD study by Dr. Miller, the Amyloid study by Dr. Jagust, and prediction of cognitive decline study by Dr. Weiner. For the epilepsy study, improved quantification of CBF and dynamic CBF measurements is expected to benefit seizure localization. For FTD and prediction of cognitive decline, VTI is expected to improve accuracy in measuring cortical thinning and loss. Better measurements of structural changes in the cortex could increase the clinical value of MRI for the diagnosis of FTD and prediction of cognitive decline towards AD in very early stages. Lastly, for the PET amyloid study, high resolution and tissue contrast of VTI is expected to benefit coregistration between structural MRI and amyloid PET data that should better the interpretation of PET results.

**E. HUMAN SUBJECTS RESEARCH**

**E.1. Protection of Human Subjects:** A "protection of human subject" section has been written for the entire application. Here, more information is provided as it related to specifics of this project.

**E.1.a. Risks to Subjects:** There appear to be no harmful biological effects of a strong static magnetic field. The major risk is from ferromagnetic objects flying into the magnet. The potential for heating of tissues from RF sources used in the MR exam is carefully controlled by SAR control devices and software that the manufacturer of the MRI scanner provides. In some subjects, there is a risk of claustrophobia, and following the study, some subjects may experience dizziness or drowsiness due to lying still for long periods of the MR exam. Some subjects may feel tired and frustrated from performing some cognitive tests while lying in the magnet. There is some risk of loss of confidentiality for participating in this research study. Involvement in the study will be voluntary and subjects can stop being in the study anytime. The alternative is not to participate.

**E.1.b. Human Subjects Involvement and Characteristics:** We will recruit healthy normal male and female subjects from 21 to 80 years old, who are able to provide informed consent. Subjects with a contraindication for MRI, such as pacemakers, ferromagnetic implants, pregnancy, unstable medical illness, claustrophobia, or an inability to cooperate with duration of MR examination will be excluded.

**E.1.c. Sources of Material:** Sources of research material will include a questionnaire for demographics data, clinical history, neuropsychologic tests, and MRI of the brain. Structural MRI, arterial-spin labeling (ASL) imaging, diffusion tensor imaging, susceptibility-weighted imaging, and intermolecular double-quantum coherence imaging will be performed for research purposes. In some cases, the MRI protocol will be repeated twice on the same day or between several days to determine short and long term reliability of the MRI measurements. Records of all tests will be stored in research binders and in a computer database. All data will be used in the research study only.

**E.1.d. Potential Risks:** A very small subset of patients may feel claustrophobic during the test. Occasionally some people experience dizziness or feel faint after lying in the magnet for a long time, but this feeling usually goes quickly away once the person gets out of the magnet.

**E.2. Adequacy of Protection Against Risks:** The subjects will have the established safety screening protocol employed at UCSF VA to assess for possible metal implants, cardiac pacers, pregnancy and other contra-indicated conditions for MR scanning. Furthermore, metal detectors are installed to prevent metal objects getting carried into the magnetic room. Subjects will be carefully monitored during all phases of their examination.

**E.2.a. Recruitment and Informed Consent:** Volunteers will be recruited by including notices in newsletters at the San Francisco Veterans Administration Medical Center, the University of California, San Francisco (UCSF), and by posting notices at other bay area colleges and universities. In addition, advertisements will be placed via the VA MR Unit webpage and in the San Francisco Chronicle Newspaper. Healthy elderly subjects will be recruited, first by identifying suitable subjects, who had MRI scans in this laboratory within the past 5 years and are in our MRI database and agreed to be contacted for research. Second, by calling these subjects if they are interested to return for an MRI; All subjects that satisfy the entry criteria will have the proposed study described, reviewing the benefits and the risks, and written informed consent will be obtained using IRB approved consent forms from UCSF and VA.

**E.2.b. Protection Against Risk:** The risk of metal flying into the MRI will be minimized by careful screening of the subject before they enter the magnet room, as well as screening of all persons entering the magnet room. The primary risk of concern is ensuring protection of patient health information. Every effort will also be made to ensure confidentiality. As patients are enrolled, a tracking number will be assigned that will be used for labeling questionnaires, information gathered from interviews, and data obtained from the medical record. Information will be stored in hard copy form at the clinical site and on a password protected computer database, both which will contain only the tracking number and no information that can be used to identify the patient.

**E.3. Potential Benefits of the Proposed Research to the Subjects and Others:** The knowledge gained from this research will be used to develop improved diagnostic techniques for assessment of neurological disorders or injury, and offers the potential of improved clinical diagnosis and monitoring outcomes of treatment trials. A potential benefit to individual subjects is reading of their MRI by a physician. In case of incidental findings, the subject will be informed by the physician about the suspected findings and instructed to contact his/her primary physician to have a clinical MRI as follow-up.

**E.4. Importance of the Knowledge to be Gained:** This study will provide information on suitability of MRI methods to detect physiological changes in the brain that might be early signs of neurodegenerative disorders, such as Alzheimer's disease and other types of dementia. This will benefit clinical application of MR technology, including early diagnosis of brain disorders and monitoring responses to treatment, if available. The study will also develop maps of cerebral blood flow in human brain. These data may provide new information on different structures in the brain, and is expected to improve the ability to detect abnormal levels of blood flow that may occur related to neurodegenerative diseases.

**E.5. Inclusion of Women and Minorities:** Women will be included in this study with equal probability as men. Pregnant women will be excluded since the potential effects of MR on the unborn child are unknown. The population recruited for this study will largely reflect the ethnic distribution of the local population. For more details on recruitment see the description in the Administrative core and The "Targeted/Planned enrollment Table".

**E.6. Inclusion of Children:** Children will not be included in this study, because the targeted brain disorders are late-onset diseases at older age. There is no scientific justification for examining the brains of children or very young adults to accomplish the goal of this study.

**F. VERTEBRATE ANIMAL:** N/A

**G. SELECT AGENT RESEARCH:** N/A

## H. LITERATURE CITED

1. Braak H, Braak E. Evolution of the neuropathology of Alzheimer's disease. *Acta Neurol Scand Suppl* 1996;165:3-12.
2. Arnold SE, Hyman BT, Flory J, Damasio AR, Van Hoesen GW. The topographical and neuroanatomical distribution of neurofibrillary tangles and neuritic plaques in the cerebral cortex of patients with Alzheimer's disease. *Cereb Cortex* 1991;1(1):103-116.
3. Feinberg DA, Kiefer B, Litt AW. High resolution GRASE MRI of the brain and spine: 512 and 1024 matrix imaging. *JComputAssistTomogr* 1995;vol.19,(no.1):1-7.
4. Feinberg DA, Kiefer B, Johnson G. GRASE improves spatial resolution in single shot imaging. *MagnResonMed* 1995;vol.33,(no.4):529-533.
5. Fu ZW, Wang Y, Grimm RC, Rossman PJ, Felmlee JP, Riederer SJ, Ehman RL. Orbital navigator echoes for motion measurements in magnetic resonance imaging. *Magn Reson Med* 1995;34(5):746-753.
6. Haase A, Frahm J, Matthaei D, H.,nicke W, Merboldt K-D. FLASH imaging. Rapid NMR imaging using low flip-angle pulses. *JMagnReson* 1986;67:258-266.
7. Mugler JP, 3rd, Brookeman JR. Three-dimensional magnetization-prepared rapid gradient-echo imaging (3D MP RAGE). *Magn Reson Med* 1990;15(1):152-157.
8. Lee JH, Garwood M, Menon R, Adriany G, Andersen P, Truwit CL, Ugurbil K. High contrast and fast three-dimensional magnetic resonance imaging at high fields. *Magn Reson Med* 1995;34(3):308-312.
9. De Vita E, Thomas DL, Roberts S, Parkes HG, Turner R, Kinches P, Shmueli K, Yousry TA, Ordidge RJ. High resolution MRI of the brain at 4.7 Tesla using fast spin echo imaging. *Br J Radiol* 2003;76(909):631-637.
10. Barbier EL, Marrett S, Danek A, Vortmeyer A, van Gelderen P, Duyn J, Bandettini P, Grafman J, Koretsky AP. Imaging cortical anatomy by high-resolution MR at 3.0T: detection of the stripe of Gennari in visual area 17. *Magn Reson Med* 2002;48(4):735-738.
11. Chakeres DW, Whitaker CD, Dashner RA, Scharre DW, Beversdorf DQ, Raychaudhury A, Schmalbrock P. High-resolution 8 Tesla imaging of the formalin-fixed normal human hippocampus. *Clin Anat* 2005;18(2):88-91.
12. Jezzard P, DUEWELL S, Balaban RS. MR relaxation times in human brain: measurement at 4 T. *Radiology* 1996;199(3):773-779.
13. Breger RK, Rimm AA, Fischer ME, Papke RA, Haughton VM. T1 and T2 measurements on a 1.5-T commercial MR imager. *Radiology* 1989;171(1):273-276.
14. Bedell BJ, Narayana PA. Volumetric analysis of white matter, gray matter, and CSF using fractional volume analysis. *Magn Reson Med* 1998;39(6):961-969.
15. Mansfield P, Morris PG. *NMR Imaging in Biomedicine*. Academic Press, New York 1982.
16. Bonny J, Durif F, Bazin JE, Touraille E, Yelnik J, Renou JP. Contrast optimization of Macaca mulatta basal ganglia in magnetic resonance images at 4.7 Tesla. *J Neurosci Methods* 2001;107(1-2):25-30.
17. Deichmann R, Good CD, Josephs O, Ashburner J, Turner R. Optimization of 3-D MP-RAGE sequences for structural brain imaging. *Neuroimage* 2000;12(1):112-127.
18. Thomas DL, De Vita E, Deichmann R, Turner R, Ordidge RJ. 3D MDEFT imaging of the human brain at 4.7 T with reduced sensitivity to radiofrequency inhomogeneity. *Magn Reson Med* 2005;53(6):1452-1458.
19. Deichmann R, Schwarzbauer C, Turner R. Optimisation of the 3D MDEFT sequence for anatomical brain imaging: technical implications at 1.5 and 3 T. *Neuroimage* 2004;21(2):757-767.
20. Boulby PA, Symms MR, Barker GJ. Optimized interleaved whole-brain 3D double inversion recovery (DIR) sequence for imaging the neocortex. *Magn Reson Med* 2004;51(6):1181-1186.
21. Hutchinson M, Raff U. Structural changes of the substantia nigra in Parkinson's disease as revealed by MR imaging. *AJNR Am J Neuroradiol* 2000;21(4):697-701.
22. Cheng HL, Wright GA. Rapid high-resolution T(1) mapping by variable flip angles: accurate and precise measurements in the presence of radiofrequency field inhomogeneity. *Magn Reson Med* 2006;55(3):566-574.
23. Wang HZ, Riederer SJ, Lee JN. Optimizing the precision in T1 relaxation estimation using limited flip angles. *Magn Reson Med* 1987;5(5):399-416.
24. Deoni SC, Rutt BK, Peters TM. Rapid combined T1 and T2 mapping using gradient recalled acquisition in the steady state. *Magn Reson Med* 2003;49(3):515-526.

25. Deoni SC, Peters TM, Rutt BK. Determination of optimal angles for variable nutation proton magnetic spin-lattice, T1, and spin-spin, T2, relaxation times measurement. *Magn Reson Med* 2004;51(1):194-199.
26. Ben-Ezra M, Zomet A, Nayar SK. Video super-resolution using controlled subpixel detector shifts. *IEEE Trans Pattern Anal Mach Intell* 2005;27(6):977-987.
27. Bertero M, Boccacci P. Super-resolution in computational imaging. *Micron* 2003;34(6-7):265-273.
28. Peled S, Yeshurun Y. Superresolution in MRI: application to human white matter fiber tract visualization by diffusion tensor imaging. *Magn Reson Med* 2001;45(1):29-35.
29. Eyal Carmi, Siuyan Liu, Noga Alon, Amos Fiat, Fiat D. Resolution enhancement in MRI. *Magnetic Resonance Imaging* 2006;24:133-154.
30. H. Greenspan, G. Oz, N. Kiryati, Peled S. MRI inter-slice reconstruction using super resolution. *Magnetic Resonance Imaging* 2002;20:437-446.
31. Greenspan H, Oz G, Kiryati N, Peled S. MRI inter-slice reconstruction using super-resolution. *Magn Reson Imaging* 2002;20(5):437-446.
32. Scheffler K. Superresolution in MRI? *Magn Reson Med* 2002;48(2):408; author reply 409.
33. Gindi G, Lee M, Rangarajan A, Zubal IG. Bayesian reconstruction of functional images using anatomical information as priors. *Medical Imaging, IEEE Transactions* 1993;12(4):670-680.
34. Hayasaka S, Du AT, Duarte A, Kornak J, Jahng GH, Weiner MW, Schuff N. A non-parametric approach for co-analysis of multi-modal brain imaging data: application to Alzheimer's disease. *Neuroimage* 2006;30(3):768-779.
35. Guenther M, Oshio K, Feinberg DA. Very Fast 3D Perfusion Measurement with High Signal-to-Noise Ratio Using Single-Shot 3D-GRASE: Application to Improve Perfusion Quantitation. 2004; Kyoto. p 714.
36. Duyn JH, van Gelderen P, Talagala L, Koretsky A, de Zwart JA. Technological advances in MRI measurement of brain perfusion. *J Magn Reson Imaging* 2005;22(6):751-753.
37. Talagala SL, Ye FQ, Ledden PJ, Chesnick S. Whole-brain 3D perfusion MRI at 3.0 T using CASL with a separate labeling coil. *Magn Reson Med* 2004;52(1):131-140.
38. Farkas E, Luiten PG. Cerebral microvascular pathology in aging and Alzheimer's disease. *Prog Neurobiol* 2001;64(6):575-611.
39. Bell MA, Ball MJ. Morphometric comparison of hippocampal microvasculature in ageing and demented people: diameters and densities. *Acta Neuropathol (Berl)* 1981;53(4):299-318.
40. Bell MA, Ball MJ. The correlation of vascular capacity with the parenchymal lesions of Alzheimer's disease. *Can J Neurol Sci* 1986;13(4 Suppl):456-461.
41. Curran EJ, Becker JB. Changes in blood-brain barrier permeability are associated with behavioral and neurochemical indices of recovery following intraventricular adrenal medulla grafts in an animal model of Parkinson's disease. *Exp Neurol* 1991;114(2):184-192.
42. Kermodé AG, Thompson AJ, Tofts P, MacManus DG, Kendall BE, Kingsley DP, Moseley IF, Rudge P, McDonald WI. Breakdown of the blood-brain barrier precedes symptoms and other MRI signs of new lesions in multiple sclerosis. Pathogenetic and clinical implications. *Brain* 1990;113 ( Pt 5):1477-1489.
43. Li KL, Zhu X, Hylton N, Jahng GH, Weiner MW, Schuff N. Four-phase single-capillary stepwise model for kinetics in arterial spin labeling MRI. *Magn Reson Med* 2005;53(3):511-518.
44. Parkes LM, Tofts PS. Improved accuracy of human cerebral blood perfusion measurements using arterial spin labeling: accounting for capillary water permeability. *Magn Reson Med* 2002;48(1):27-41.
45. St Lawrence KS, Frank JA, McLaughlin AC. Effect of restricted water exchange on cerebral blood flow values calculated with arterial spin tagging: a theoretical investigation. *Magn Reson Med* 2000;44(3):440-449.
46. de Bazelaire C, Rofsky NM, Duhamel G, Zhang J, Michaelson MD, George D, Alsop DC. Combined T2\* and T1 measurements for improved perfusion and permeability studies in high field using dynamic contrast enhancement. *Eur Radiol* 2006.
47. Detre JA, Leigh JS, Williams DS, Koretsky AP. Perfusion imaging. *MagnResonMed* 1992;23(1):37-45.
48. Kim SG. Quantification of relative cerebral blood flow change by flow-sensitive alternating inversion recovery (FAIR) technique: application to functional mapping. *MagnResonMed* 1995;34(3):293-301.
49. Calamante F, Williams SR, van Bruggen N, Kwong KK, Turner R. A model for quantification of perfusion in pulsed labelling techniques. *NMR Biomed* 1996;9(2):79-83.
50. Alsop DC, Detre JA. Reduced transit-time sensitivity in noninvasive magnetic resonance imaging of human cerebral blood flow. *J Cereb Blood Flow Metab* 1996;16(6):1236-1249.

51. Buxton RB, Frank LR, Wong EC, Siewert B, Warach S, Edelman RR. A general kinetic model for quantitative perfusion imaging with arterial spin labeling. *Magn Reson Med* 1998;40(3):383-396.
52. Zhou J, van Zijl PC. Effect of transit times on quantification of cerebral blood flow by the FAIR T(1)-difference approach. *Magn Reson Med* 1999;42(5):890-894.
53. Ewing JR, Cao Y, Fenstermacher J. Single-coil arterial spin-tagging for estimating cerebral blood flow as viewed from the capillary: relative contributions of intra- and extravascular signal. *Magn Reson Med* 2001;46(3):465-475.
54. Zhou J, Wilson DA, Ulatowski JA, Traystman RJ, van Zijl PC. Two-compartment exchange model for perfusion quantification using arterial spin tagging. *J Cereb Blood Flow Metab* 2001;21(4):440-455.
55. Eichling JO, Raichle ME, Grubb RL, Jr., Ter-Pogossian MM. Evidence of the limitations of water as a freely diffusible tracer in brain of the rhesus monkey. *Circ Res* 1974;35(3):358-364.
56. Gjedde A, Andersson J, Eklof B. Brain uptake of lactate, antipyrine, water and ethanol. *Acta Physiol Scand* 1975;93(2):145-149.
57. Herscovitch P, Markham J, Raichle ME. Brain blood flow measured with intravenous H<sub>2</sub>(<sup>15</sup>O). I. Theory and error analysis. *J Nucl Med* 1983;24(9):782-789.
58. Raichle ME, Eichling JO, Straatman MG, Welch MJ, Larson KB, Ter-Pogossian MM. Blood-brain barrier permeability of <sup>11</sup>C-labeled alcohols and <sup>15</sup>O-labeled water. *Am J Physiol* 1976;230(2):543-552.
59. Koeppe RA, Hutchins GD, Rothley JM, Hichwa RD. Examination of assumptions for local cerebral blood flow studies in PET. *J Nucl Med* 1987;28(11):1695-1703.
60. Barbier EL, Silva AC, Kim SG, Koretsky AP. Perfusion imaging using dynamic arterial spin labeling (DASL). *Magn Reson Med* 2001;45(6):1021-1029.
61. Li K-L, Zhu X-P, Jahng G-H, Hylton N, Weiner MW, Schuff N. A Four-Phase Single-Capillary Stepwise Model for Kinetics in Arterial Spin Label MRI. *Magn Reson Imaging* 2005;53:000-000.
62. Pruessmann KP, Weiger M, Scheidegger MB, Boesiger P. SENSE: sensitivity encoding for fast MRI. *Magn Reson Med* 1999;42(5):952-962.
63. Studholme C, Constable RT, Duncan JS. Constraining Non-Rigid Registration Of EPI to Conventional MRI using a Distortion Model. 2000 2000//International Society of Magnetic Resonance in Medicine, 7th Annual Meeting, Philadelphia, May 22-28, 1999.
64. Kybic J, Thevenaz P, Nirkko A, Unser M. Unwarping of unidirectionally distorted EPI images. *IEEE Trans Med Imaging* 2000;19(2):80-93.
65. Rohde GK, Barnett AS, Basser PJ, Marengo S, Pierpaoli C. Comprehensive approach for correction of motion and distortion in diffusion-weighted MRI. *Magn Reson Med* 2004;51(1):103-114.
66. Ardekani S, Sinha U. Geometric distortion correction of high-resolution 3 T diffusion tensor brain images. *Magn Reson Med* 2005;54(5):1163-1171.
67. Munger P, Crelier GR, Peters TM, Pike GB. An inverse problem approach to the correction of distortion in EPI images. *IEEE Trans Med Imaging* 2000;19(7):681-689.
68. Jezzard P, Balaban RS. Correction for geometric distortion in echo planar images from B<sub>0</sub> field variations. *Magn Reson Med* 1995;34(1):65-73.
69. Macovski A. Volumetric NMR imaging with time-varying gradients. *Magn Reson Med* 1985;2(1):29-40.
70. Sutton BP, Noll DC, Fessler JA. Fast, iterative image reconstruction for MRI in the presence of field inhomogeneities. *IEEE Trans Med Imaging* 2003;22(2):178-188.
71. Kadah YM, Hu X. Simulated phase evolution rewinding (SPHERE): a technique for reducing B<sub>0</sub> inhomogeneity effects in MR images. *Magn Reson Med* 1997;38(4):615-627.
72. Zeng H, Constable RT. Image distortion correction in EPI: comparison of field mapping with point spread function mapping. *Magn Reson Med* 2002;48(1):137-146.
73. Andersson JL, Skare S, Ashburner J. How to correct susceptibility distortions in spin-echo echo-planar images: application to diffusion tensor imaging. *Neuroimage* 2003;20(2):870-888.
74. Chang H, Fitzpatrick JM. A technique for accurate MR imaging in the presence of field inhomogeneities. *IEEE Trans Med Imaging* 1992;11:319-329.
75. Itakura F. Minimum prediction residual principle applied to speech recognition. *IEEE Trans Acoust Speech Signal Processing* 1975;23(67-72).
76. Kannengiesser SA, Wang Y, Haacke EM. Geometric distortion correction in gradient-echo imaging by use of dynamic time warping. *Magn Reson Med* 1999;42(3):585-590.

77. Haupt CI, Schuff N, Weiner MW, Maudsley AA. Removal of lipid artifacts in 1H spectroscopic imaging by data extrapolation. *Magnetic Resonance in Medicine* 1996;35:678-687.
78. Schuff N, Ezekiel F, Gamst A, Amend D, Capizzano A, Maudsley AA, Weiner MW. Region and tissue differences of metabolites in normally aged brain using 1H magnetic resonance spectroscopic imaging. *MagnResonMed* 2001;45:899-907.
79. Chao LL, Schuff N, Kramer JH, Du AT, Capizzano AA, O'Neill J, Wolkowitz OM, Jagust WJ, Chui HC, Miller BL, Yaffe K, Weiner MW. Reduced medial temporal lobe N-acetylaspartate in cognitively impaired but nondemented patients. *Neurology* 2005;64(2):282-289.
80. Jahng G, Zhu X, Matson G, Weiner M, Schuff N. Novel Double Inversion of Both Tagged and Reference Images For Pulsed Arterial Spin Labeling. 2002.
81. Jahng GH, Song E, Zhu, X.P., Matson, G.P., Weiner, M.W., Schuff, N. Global and Regional Reliability and Reproducibility of Pulsed Arterial Spin Labeled Perfusion MRI in the Human Brain. *Radiology* 2005;205(234):909-910.
82. Jahng GH, Zhu XP, Matson GB, Weiner MW, Schuff N. Improved perfusion-weighted MRI by a novel double inversion with proximal labeling of both tagged and control acquisitions. *Magn Reson Med* 2003;49(2):307-314.
83. Mueller SG, Du A-T, Stables L, Schuff N, Sacrey D, Cashdollar N, Weiner MW. Measurement of Hippocampal Subfields and Age-related Changes with High Resolution MRI at 4Tesla. 2005; Washington DC.
84. Ebel A, Maudsley AA, Schuff N, Weiner MW. Achieving Sufficient Spectral Bandwidth for Volumetric 1H Echo-Planar Spectroscopic Imaging at 4 Tesla. *Magn Reson Imaging* 2005;In Press.
85. Griswold MA, Jakob PM, Heidemann RM, Nittka M, Jellus V, Wang J, Kiefer B, Haase A. Generalized autocalibrating partially parallel acquisitions (GRAPPA). *Magn Reson Med* 2002;47(6):1202-1210.
86. Bell AJ, Sejnowski TJ. An information-maximization approach to blind separation and blind deconvolution. *Neural Comput* 1995;7(6):1129-1159.
87. Wong EC, Buxton RB, Frank LR. Implementation of quantitative perfusion imaging techniques for functional brain mapping using pulsed arterial spin labeling [see comments]. *NMR Biomed* 1997;10(4-5):237-249.
88. Edelman RR, Siewert B, Darby DG, Thangaraj V, Nobre AC, Mesulam MM, Warach S. Qualitative mapping of cerebral blood flow and functional localization with echo-planar MR imaging and signal targeting with alternating radio frequency. 1994;192(2):513-520.
89. Edelman RR, Chen Q. EPISTAR MRI: multislice mapping of cerebral blood flow. *MagnResonMed* 1998;40(6):800-805.
90. Haralick RM, Shanmugam K, Dinstein L. Texture features for image classification. *IEEE Trans Syst Man Cybernet* 1973;3:610-621.
91. Jahng GH, Stables L, Ebel A, Matson GB, Meyerhoff DJ, Weiner MW, Schuff N. Sensitive and fast T1 mapping based on two inversion recovery images and a reference image. *Med Phys* 2005;32(6):1524-1528.
92. Stocker T, Shah NJ. MP-SAGE: A new MP-RAGE sequence with enhanced SNR and CNR for brain imaging utilizing square-spiral phase encoding and variable flip angles. *Magn Reson Med* 2006;56(4):824-834.
93. Hsu JJ, Glover GH. Rapid MRI method for mapping the longitudinal relaxation time. *J Magn Reson* 2006;181(1):98-106.
94. Dey N, Blanc-Feraud L, Zimmer C, Roux P, Kam Z, Olivo-Marin JC, Zerubia J. Richardson-Lucy algorithm with total variation regularization for 3D confocal microscope deconvolution. *Microsc Res Tech* 2006;69(4):260-266.
95. Snyder DL, Schulz TJ, O' Sullivan JA. Deblurring subject to nonnegativity constraints. *IEEE Transactions on Signal Processing* 1992;40(5):1143-1150.
96. Hadjidemetriou S, Studholme C, Mueller S, Weiner M, Schuff N. Restoration of MRI data for field nonuniformities using high order neighborhood statistics. 2007; San Diego.
97. De Vita E, Thomas D, Deichmann R, Turner R, Ordidge R. Fast B1 mapping with EPI. *Proc Intl Soc Mag Reson Med* 2004;11:2090.

Principal Investigator/Program Director (Last, First, Middle): Weiner, Michael W.

98. Zhu XP, Du AT, Jahng GH, Soher BJ, Maudsley AA, Weiner MW, Schuff N. Magnetic resonance spectroscopic imaging reconstruction with deformable shape-intensity models. *Magn Reson Med* 2003;50(3):474-482.
99. Dennie J, Mandeville JB, Boxerman JL, Packard SD, Rosen BR, Weisskoff RM. NMR imaging of changes in vascular morphology due to tumor angiogenesis. *Magn Reson Med* 1998;40(6):793-799.
100. Hayashida K, Tanaka Y, Hirose Y, Kume N, Iwama T, Miyake Y, Ishida Y, Matsuura H, Nishimura T. Vasoreactive effect of acetazolamide as a function of time with sequential PET 15O-water measurement. *Nucl Med Commun* 1996;17(12):1047-1051.
101. Ashburner J, Friston KJ. Voxel-based morphometry--the methods. *Neuroimage* 2000;11(6 Pt 1):805-821.
102. de Oliveira MC, Kitney RI. Texture analysis for discrimination of tissues in MRI data. *Computers in Cardiology*; 1992. p 481-484.